

LA-UR-17-20105 (Accepted Manuscript)

Location of intense electromagnetic ion cyclotron (EMIC) wave events relative to the plasmapause: Van Allen Probes observations

Tetrick, S. S.; Engebretson, M. J.; Posch, J. L.; Olson, C. N.; Kletzing, C. A.; Smith, C. W.; Thaller, S. A.; Wygant, J. R.; Reeves, Geoffrey D.; MacDonald, E. A.; Fennell, J. F.

Provided by the author(s) and the Los Alamos National Laboratory (2017-10-17).

To be published in: Journal of Geophysical Research: Space Physics

DOI to publisher's version: 10.1002/2016JA023392

Permalink to record: http://permalink.lanl.gov/object/view?what=info:lanl-repo/lareport/LA-UR-17-20105

Disclaimer

Approved for public release. Los Alamos National Laboratory, an affirmative action/equal opportunity employer, is operated by the Los Alamos National Security, LLC for the National Nuclear Security Administration of the U.S. Department of Energy under contract DE-AC52-06NA25396. Los Alamos National Laboratory strongly supports academic freedom and a researcher's right to publish; as an institution, however, the Laboratory does not endorse the viewpoint of a publication or guarantee its technical correctness.



- Location of intense electromagnetic ion cyclotron (EMIC) wave events
- relative to the plasmapause: Van Allen Probes observations

4

3

- 5 S. S. Tetrick¹, M. J. Engebretson¹, J. L. Posch¹, C. N. Olson¹, C. A. Kletzing², C. W. Smith³, S.
- 6 A. Thaller⁴, J. R. Wygant⁴, G. D. Reeves⁵, E. A. MacDonald⁶, and J. F. Fennell⁷

7

8

- 9 ¹Augsburg College, Minneapolis, MN
- 10 ²University of Iowa, Iowa City, IA
- 11 ³University of New Hampshire, Durham, NH
- ⁴University of Minnesota, Minneapolis, MN
- ⁵Los Alamos National Laboratory, Los Alamos, NM
- 14 ⁶NASA Goddard Space Flight Center, Greenbelt, MD
- ⁷The Aerospace Corporation, Los Angeles, CA

16

- submitted to the Journal of Geophysical Research Space Physics
- 18 August 25, 2016

Abstract

19

20

21

22

23

24

25

26

27

28

29

30

31

32

33

34

35

36

We have studied the spatial location relative to the plasmapause (PP) of the most intense electromagnetic ion cyclotron (EMIC) waves observed on Van Allen Probe A from October 1, 2012 through the end of 2014. Most of these waves occurred over an L range of from -1 to +2 R_E relative to the PP. Very few events occurred only within 0.1 R_E of the PP, and events similarly narrow in L occurred both inside and outside the PP. Wave occurrence was always associated with high densities of ring current ions; plasma density gradients or enhancements were associated with some events but were not dominant factors in determining the sites of wave generation. Storm main and recovery phase events in the dusk sector were often inside the PP, and dayside events during quiet times and compressions were more evenly distributed both inside and outside the PP. Superposed epoch analyses of the dependence of wave onset on solar wind dynamic pressure (Psw), the SME (SuperMAG auroral electrojet) index, and the Dst index showed that substorm injections and solar wind compressions were temporally closely associated with EMIC wave onset, but to an extent that varied with frequency band, MLT, storm phase, and location relative to the PP. Events related most clearly to solar wind compressions were mainly observed outside the PP (but also included H band events at the PP), while events related most clearly to substorm injections were mainly located inside the PP (but also included He band events at the PP).

1. Introduction

37

38

39

40

41

42

43

44

45

46

47

48

49

50

51

52

53

54

55

56

57

58

Electromagnetic ion cyclotron (EMIC) waves come from a class of ultra-low frequency (ULF) Pc1-2 (0.1 - 5 Hz) frequency range pulsations and are transverse, left-handedly polarized. EMIC waves need an anisotropic $(T_{\perp} > T_{\parallel})$ and energetic/hot (10 - > 100 keV) ion population to be generated. There have been theoretical studies that suggest an enhancement of cold dense plasma is needed for EMIC generation and wave growth rate [Cornwall et. al., 1970; Kozyra et. al., 1984]. This cold plasma has been suggested to be associated with the plasmasphere or plasmaspheric plumes. The energetic hot ion population, commonly identified as the ring current, can be injected into the inner magnetosphere during geomagnetic storms and substorms [Reeves and Henderson, 2001]. This hot ion population provides the free energy necessary for EMIC wave growth, and can drift to encounter the cold plasmasphere ion populations [Cornwall, 1965; Jordanova et. al, 2001]. However, a recent study by Gkioulidou et al. [2016] provided evidence that the dynamics of the lower energy ring current ($\leq 80 \text{ keV}$) are different from those of the higher energy ring current > 100 keV), in that inward transport of the former is primarily "convective," driven by a large-scale convection electric field and particle injections, while the latter is largely diffusive, with much longer time scales. In particular, Gkioulidou et al. [2016] showed that while the lower energy ring current population was correlated with Sym-H index values, the high-energy ring current proton population (≥ 100 keV) had no correlation, or even an anticorrelation, with Sym-H.

EMIC waves are suspected to play a key role in energetic particle loss through wave particle interactions [Cornwall et. al., 1970; Lyons et. al., 1972]. If EMIC waves occur over multiple magnetic local times (MLTs) and L shells, they could potentially have global effects.

EMIC waves also have the ability to deplete the highly relativistic electron population of the outer radiation belt [e.g. Usanova et al., 2014; Engebretson et al., 2015].

Many theoretical studies have predicted that the plasmapause (PP) and plasmaspheric plumes would be a preferred location for the generation of EMIC waves, both because of the often-observed confluence of ring current ions and increased levels of cold plasma, and because the sharp PP density gradient would help guide the waves along the magnetic field, allowing bouncing wave packets to grow during successive equatorial crossings (see for example, the review of Halford et al. [2015]).

Neither the bouncing wave packet model nor the preference for generation at the PP gradient have received much support in the past two decades, however. Satellite-ground studies by Mursula et al. [2001], Mursula [2007], and Usanova et al. [2008], for example, have all cast doubt on the bouncing wave packet model.

Of more relevance to this study, however, is the location of EMIC waves relative to the PP, as reported by numerous elliptically-orbiting spacecraft. When the first large-scale study of equatorial Pc1-2 waves was conducted by Anderson et al. [1992a, 1992b] using observations from the Charge Composition Explorer (CCE) in the Active Magnetospheric Particle Tracer Explorers (AMPTE) mission, EMIC waves were found to occur for L > 8 more often than at L values ≤ 7 . This result was in opposition to a previous study by Kaye and Kivelson [1979] that found EMIC waves to be rare beyond L = 7 (based on OGO 5 data). Anderson et al. [1992a] concluded that the Kaye and Kivelson study did not look at frequency ranges low enough (less than 0.1 Hz) to detect the waves at higher L values. Usanova et al. [2016], using data from the Cluster spacecraft, also found EMIC wave occurrence increased with L shell, consistent with

other studies done using THEMIS data [Usanova et al., 2012; Min et al., 2012] and AMPTE CCE data [Anderson et al., 1992; Keika et al., 2013]. These studies suggested that steep PP gradients may not be major factor in EMIC wave generation.

Several of the above studies have also suggested that EMIC wave generation becomes more favorable during compressions in the magnetic field caused by solar wind dynamics, which then causes the plasma to become unstable. Increases in solar wind dynamic pressure can increase the temperature anisotropies of ring current ions within the magnetosphere, so EMIC wave generation can occur in regions of lower density as well [Anderson and Hamilton, 1993; Arnoldy et al., 2005; Usanova et al., 2010; 2013]. Dayside compressions in the magnetosphere can allow for an optimum environment for EMIC wave generation due to the resulting more anisotropic distribution of ions [Tsurutani and Smith, 1966; McCollough et al., 2012; Usanova et al., 2012]. However, several recent studies have connected compressions to increased proton precipitation, most likely linked to EMIC waves, which can occur even in the nighttime sector (Meurant et al. [2003]; Lee et al. [2005, 2007]; Zhang et al. [2005, 2008]; Søraas et al. [2013]). Evidence has also been presented indicating that solar wind dynamic pressure influences relativistic electron precipitation events, driven by EMIC waves, more than geomagnetic activity [Wang et al., 2014].

Observational support for EMIC wave generation over a variety of L shells has been backed by statistical studies that found only slight enhancement in wave occurrence near the PP [Anderson et al., 1992a; Keika et al., 2013; Fraser and Nguyen, 2001]. In particular, Fraser and Nguyen [2001] found using CRRES spacecraft data that EMIC wave events were observed over

a wide range of L values relative to the PP (see especially their Figure 13), indicating the PP is not the preferred location of wave generation.

However, few more recent studies have looked in detail at the spatial location of wave generation relative to PP density gradients. A recent study of EMIC waves by Wang et al. [2015] using Van Allen Probes data concluded that most events were located near the PP; 37% of events were identified outside the plasmasphere, and 63% inside the plasmasphere. However, in a recent case study by Zhang et al. [2013], 3 EMIC wave events were observed on Van Allen Probe A on April, 28, 2013. All three of the events occurred near the PP; wave #3 had a distinct drop in n_e (clear PP location), while waves #1 and #2 both had more gradual drops, but all three were associated with decreasing n_e values. Although steep PP density gradients may provide conditions that enhance the growth of EMIC waves, and EMIC wave occurrence can certainly be observed there, location at the PP is evidently not a requirement for EMIC instability. Recent observational and theoretical studies supporting this point will be cited below.

In this study we provide a more quantitative definition of "near the PP" for EMIC waves in four local time sectors, in three frequency bands (H, He, and both), and for various phases of magnetic storms, based on Van Allen Probe A observations. Because the apogee of Van Allen Probe A is lower (5.8 R_E) than that of the equatorially orbiting spacecraft used in previous surveys of EMIC waves (AMPTE CCE at 8.8 R_E , CRRES at 6.3 R_E , and THEMIS at 10 R_E) it spends a greater fraction of each orbit traversing the inner magnetosphere. As Saikin et al. [2015] noted, this may be one reason why the occurrence patterns reported in their recent Van Allen Probe survey differ from those of earlier statistical studies.

It is generally accepted that EMIC waves in the equatorial region are able to cause pitch angle scattering and precipitation of ring current protons, which ultimately leads to ring current decay. One of the reasons why the PP is assumed to be the preferred region for generation of EMIC waves is because during storm recovery phases, the cold PP overlaps with the hot ring current and provides ideal conditions for wave generation and propagation, explaining why the study of EMIC waves in relation to geomagnetic storms is important. Many studies have been done relating EMIC wave generation to storm phases on various satellite missions. Fraser et al. [2010] analyzed a total of 13 storms, and found that EMIC wave occurrences during the main phase of storms at geosynchronous (GEO) orbit were only 29% of the total events. An earlier study by Erlandson and Ukhorskiy [2001], using DE-1 magnetic field data, found EMIC waves were about 5 times more likely to occur during the main and recovery phases of a geomagnetic storm when compared to quiet phases, but their statistical results were dominated by one large storm. Saikin et al. [2016], using Van Allen Probe data, found EMIC wave occurrence was more likely to be observed in the recovery phase of geomagnetic storms compared to the main phase, disagreeing with the Halford et al. [2010] study that found 58% of EMIC waves were observed during the main phase. The discrepancy could be due to the differences in solar cycles because the two satellites were separated by about 20 years, and possibly also because CRRES data coverage did not extend to all local times (in particular, it provided little data in the dawn to noon quadrant). Studies showing that EMIC waves appear in ground records more frequently during recovery phases go back to the 1960s (as reviewed by Engebretson et al., [2008]). This current study will distinguish between storm phases, and show several examples that highlight the complex patterns in ion populations associated with these waves under varying levels of geomagnetic activity.

123

124

125

126

127

128

129

130

131

132

133

134

135

136

137

138

139

140

141

142

143

144

145

This paper is organized in the following way: a description of the instrumentation of the Van Allen Probes and the techniques involved in the data analysis for this study (section 2), seven examples of EMIC wave events (section 3), statistical results sorted by local time sector, frequency band, storm phase, and location relative to the plasmapause (section 4), superposed epoch analyses of wave occurrence as a function of Psw, SME, and Dst (section 5), presentation of the spatial distribution of RMS wave amplitudes (section 6), and discussion and conclusions (section 7).

2. Instrumentation and Technique

2.1 Van Allen Probes

The Van Allen Probes mission (originally designated Radiation Belt Storm Probes, RBSP) consists of two identical spacecraft (denoted as A and B) that are both in highly elliptical and low inclination ($\sim 10^{\circ}$) orbits with perigee of 1.1 Earth radii (R_E) and apogee of $5.8R_E$. Both Probes A and B follow approximately the same trajectory, but at two different speeds. This means that one probe will overlap the other about every 2.5 months. The probes take identical measurements, consisting of magnetic field (B), electric field (E), waves, and particle parameters (electrons, ions, and ion composition). This current study consists of data observed by only probe A from its launch through the end of 2014, during which interval it precessed through all local times. This study used data from the Van Allen Probes' Electric and Magnetic Field Instrument Suite and Integrated Science (EMFISIS) fluxgate magnetometer, which measures 64 vector samples/s of the vector magnetic field, giving a Nyquist rate of 32 Hz [Kletzing et al., 2013]. Plots of the EMFISIS data were created for each day and the EMIC waves were then visually identified. This study also used simultaneous electron density data obtained by the Electric Fields

and Waves (EFW) instrument. The EFW instrument measures the vector electric field at a rate of 32 vector samples/s, which gives a Nyquist rate of 16 Hz [Wygant et al., 2013]. Spacecraft potential measurements obtained by the EFW spin plane booms were also used to determine the local electron density. Data for solar wind parameters were taken from the OMNI dataset, which consists of upstream solar wind data time-shifted to its expected arrival at Earth's bow shock.

Ring current ions were measured using two instruments that are part of the Energetic Particle, Composition, and Thermal Plasma (ECT) suite [Spence et al., 2013] on each Van Allen Probe spacecraft. Ions with energies from ≤ 20 eV or spacecraft potential (whichever is greater) to ≥ 45 keV were measured by the ECT/HOPE (Helium Oxygen Proton Electron) mass spectrometer instrument [Funsten et al., 2013]. Ions with energies from 50 keV to greater than 1 MeV were measured by the ECT/MagEIS (Magnetic Electron Ion Spectrometer) silicon detector telescope [Blake et al., 2013]. This telescope has no composition discrimination but the fluxes will be dominated by protons.

2.2 Data Analysis

In this study we surveyed all the EMIC waves observed by the EMFISIS fluxgate magnetometer on Van Allen Probe A from October 1, 2012 through the end of 2014, and selected 78 of the most intense wave events for analysis. For each event we also examined simultaneous electron density data obtained by the Electric Fields and Waves (EFW) instrument in order to identify the location of a plasmapause or other density structure (e.g., a plasmaspheric plume). In order for an event to be included in our statistical study of event locations relative to the plasmapause, we specified that it must satisfy the following three criteria: a) the plasmapause must have been encountered within 2 hours of the wave event, b) the electron

density must have crossed the 50 cm⁻³ density level, and c) a clear rise or drop was observed over a short time (so that a PP time could be specified to within ~5 minutes). In several cases of an expanded plasmasphere, the electron density remained above 50 cm⁻³ throughout an entire orbit, so no plasmapause was encountered. A total of 55 wave events satisfied all three criteria, but the wave event shown in Figure 2 and the first event in Figure 3 did not meet all of these criteria, so these and similar events were excluded from the PP analysis. Table 1 shows the number of events in this study, categorized by location relative to the plasmapause, by storm phase, and by local time sector.

In order to examine EMIC wave occurrence in relation to storm activity, each wave event was categorized by its respective storm phase: pre-onset, main, recovery, quiet, and compression, based on the Dst index, using the same set of definitions for storm phase events used by Halford et al. [2010] and Saikin et al. [2016]. The pre-onset storm phase was 3 hours prior to the onset of a storm, main phase was described as the onset of a storm until the Sym-H reached its minimum and the slope then changed to positive, and recovery phase was from the end of the main phase until Sym-H recovered 80% of the minimum value reached during the storm, or until the onset of the next storm.

The timing of EMIC wave events was also analyzed relative to three magnetic indices (AE, SME, and Dst) and solar wind pressure (Psw) and its variation (ΔPsw, based on 5-min OMNI Psw data). We performed superposed epoch analyses of wave onset as a function of each of these variables in order to investigate possible temporal associations of EMIC wave events (grouped by location relative to the PP, MLT sector, and storm phases) with substorm injections

(increases in AE and SME), ring current intensity (level of Dst), and solar wind-induced magnetospheric compressions (increase in Dst, Psw, and Δ Psw).

In addition to the widely-used AE auroral electrojet index, based on 12 auroral zone stations, we produced plots using the SME SuperMAG auroral electrojet index, which typically incorporates data from 100 stations at geomagnetic latitudes between +40 and +80 degrees [Newell and Gjerloev, 2011]. Newell and Gjerloev [2011] documented that SME, derived at a 1-min cadence, captures a significant amount of auroral activity and substorm activations that the AE index misses because of its coarser spatial coverage. Comparison of superposed epoch plots using AE and SME indicated that the SME index showed slightly more activity and temporal variation, and in many instances ~100 nT higher values near wave onset, so only SME values will be shown here.

Wave events were also characterized by frequency band. When an EMIC wave event occurred below the proton gyrofrequency and above the helium ion gyrofrequency, it was considered to be in the hydrogen-band. If the wave occurred below the helium ion gyrofrequency and above the oxygen ion gyrofrequency, then it was categorized as being in the helium-band. If the wave occurred below the oxygen ion gyrofrequency it was categorized as being in the oxygen-band. No oxygen-band events, however, were observed in this study. Each EMIC wave event was identified visually and the start and end times were recorded. Once all EMIC wave events were identified and recorded, then each event was sorted by its frequency band (hydrogen, helium, or both).

3. Examples Sorted by Storm Phase

In this section we show seven examples of EMIC waves and simultaneous observations of electron densities and fluxes of ring current protons. Only spin-averaged fluxes are shown here, but during each event the angular distribution of fluxes of particles at energies temporally associated with the waves was strongly anisotropic, with peak fluxes at pitch angles near 90° (not shown).

3.1 Recent injections

Figure 1 shows Van Allen Probe A data during an outbound pass from 16 to 20 h UT November 30, 2014, centered on an EMIC wave event in both the H and He bands between 17:50 and 18:00 UT (panel a) that occurred at and slightly inside a sharp plasmapause near L \sim 4.9, evident in the electron density (panel b) shortly after midnight local time. The peak amplitudes of this wave event were 1.5 nT in the He and 2 nT in the H band. The spurious constant tone at 1.4 Hz was produced by a heater near the sensor. A strong substorm injection (AE \sim 700) occurred 1 hour before this wave event, during an extended storm recovery period 14 days after the most recent prior storm (SYM-H \sim +10).

Ring current proton fluxes measured by the HOPE instrument (panel c) had maximum intensity in the energy range from 2 to 9.6 keV and were anisotropic (peaked near 90°) at just the time of the event. 21 keV ions had an intensity peak of short duration, from 18:00 to 18:10, just after the wave event ended. Fluxes dropped sharply above 21 keV in the HOPE data, and unfortunately MagEIS data in the 58 to 118 keV range were not available at either Van Allen Probe A or B during this interval. MagEIS ion fluxes from 164 keV and up (panel d) were also sharply peaked at 90°, and decreased steadily from 17:30 to 18:20, but no feature in this higher energy range corresponded in time to the wave event.

Figure 2 shows Van Allen Probe A data from 10:00 to 14:00 UT September 24, 2013, during which EMIC waves occurred on an inbound pass from \sim 19 to \sim 22 hours MLT as the spacecraft passed from L = 5 to 3.5 during the main phase of a weak storm (minimum Dst = -30 nT at 12:35 UT) after 21 days of quiet conditions. The AE index peaked near 800 nT at 11:15 and 12:20 UT. Panel a shows an extended EMIC wave event from 11:38 to 12:35 UT and another more intense event from 12:44 to 12:49 UT. The peak amplitudes of these wave events, both in the He band, were 8 nT and 21 nT respectively. The waves occurred deep inside an expanded plasmasphere (which extended to high L (> 6) in a region where n_e increased from 200 to 800 cm⁻³(panel b)).

Ring current fluxes at different energies peaked at different times in the HOPE and MagEIS data sets. The HOPE data (panel d) shows that proton fluxes were elevated and moderately anisotropic at energies ranging from 3 keV to 52 keV from 11:10 to 12:55 UT, and 20-30 keV protons were most intense near 12:47 UT, the time of the strongest event. The flux of cool plasma (<10 eV) increased during this interval, but the electron density (indicative of the cold plasma density) showed a slight decrease. Significant fluxes of He⁺ and O⁺ were also present from 11:10 to 12:57 (including the time of both wave events). A gap in EMIC wave power near 12:40 UT coincided with a drop in 4.5 to ~30 keV proton fluxes and with a drop in cool plasma flux (< 10 eV), but with a small increase ("antiplume") in electron density. Fluxes at all energies from 10 eV to 52 keV dropped sharply after 13:00 UT. MagEIS fluxes (panel c) at all available energies (58 keV to 1271 keV) were anisotropic. Fluxes between 82 and 118 keV peaked between 11:40 and 12:40 UT, and the fluxes between 164 and 229 peaked between 12:40 and 12:50, at the time of the second (stronger) wave event.

No significant fluxes of plasmasheet (0.1 - 1 keV) ions were observed during either of these events.

3.2. Early storm recovery (4-6 hours after end of main phase)

Figure 3 shows Van Allen Probe A data during an outbound pass in the afternoon sector from 12:00 to 16:00 UT November 11, 2013 during the early recovery phase of a magnetic storm with minimum Dst = -70 nT at 08:00 UT. Panel a shows two EMIC wave events, the first in both H and He bands (with peak amplitudes of 0.7 nT in the H band and 2 nT in the He band) from 12:45 to 13:11 UT, and the second from 14:36 to 14:50 UT in the He band, with peak amplitude 4 nT. The first event occurred near L \sim 4 in a region of nearly constant plasma density just outside a very gradual drop in cold plasma density (plasmapause), and the second inside a region of elevated cold plasma density (a plume) near L \sim 5.5.

Ring current fluxes during the 4-hour period shown in panels c (MagEIS) and d (HOPE) of Figure 3 exhibited complex variations. The first wave event coincided with the lowest-L extent of increased fluxes in the ~6 to ~30 keV range (panel d), which peaked between ~12:50 and 13:10 UT, and with increased fluxes in the ~150 keV range (panel c). The second wave event coincided with an intensification of protons near 10 keV (panel d). Panel d also shows that the interval of enhanced electron density from 14:30 to 14:55 shown in panel b was bounded by increased densities of warm plasma (up to 100 eV) at 14:30 and 14:55 UT. Fluxes at considerably higher energies, between 82 and 308 keV (panel c), were elevated between 14:24 and 14:56, an interval similar to, but slightly wider than, the interval of increased electron densities (plume) and cool plasma within which the wave event was embedded. We note that neither of these wave events occurred in regions of spatial density gradients.

Figure 4 shows Van Allen Probe A data from 08:00 to 12:00 UT June 29, 2013, during the early recovery phase of a magnetic storm with minimum Dst values of -98 nT at 02:00 and 07:00 UT. EMIC wave events occurred during both the inbound and outbound passes on this day, during which the PP was at very low L (panel b). The first (H band) event, with peak amplitude of 1 nT, occurred from 08:52 to 09:00 UT, shortly after midnight local time near L \sim 3.6, more than 1 R_E outside the PP, and was coincident with a short-lived increase in Psw from \sim 4 to 6 nPa. The AE index was near 800 nT for \sim 2 hours prior to this event. During the subsequent outbound pass near 18 MLT a set of three temporally / spatially limited wave events occurred at two inner edges and one outer edge of a plume at 11:24, 11:26, and 11:30 UT, respectively, between L \sim 3.2 and \sim 3.4. Peak amplitudes of the 11:24 UT event were 8 nT in the He band and 1.5 nT in the H band. Peak amplitude of the 11:26 event (in the H band) was 0.8 nT, and peak amplitudes of the 11:30 UT event were 10 nT in the He band and 0.6 nT in the H band. During this second event AE ranged from 1500 to 2500 nT, indicating strong injections. During both events there was a large flux of ring current helium ions (not shown).

The first wave event (from 08:52 to 09:00 UT) coincided with peak fluxes in MagEIS data between ~110 and ~200 keV (panel c). Fluxes at lower energies (20 keV to 110 keV), shown in panels c and d, were also elevated during this time, but reached their highest values several minutes after the waves had ended.

The wave bursts between 11:24 and 11:30 UT coincided with increases in fluxes over a wide range of energies. Ion fluxes at energies from ~160 keV up to ~350 keV (panel c) increased sharply to near maximum values at 11:22, and remained high until 11:45 UT. Ions from ~40 to ~160 keV (panels c,d) increased slightly earlier, near 11:20 UT, and remained at high values several minutes longer. Fluxes of ions between 10 keV and 40 keV increased

slightly earlier (beginning at 11:05 UT at 30 keV), and remained high to 12:00 UT and beyond. The first wave burst near 11:22 occurred simultaneously with the intensification of > 160 keV ions, and the second and third bursts, near 11:26 and 11:30 UT, occurred while these fluxes remained high. Sharp increases in the fluxes of < 100 eV ions (panel d) also occurred near 11:24 UT and 11:30 UT, coincident with the inner (rising) and outer (falling) edges of the plume evident in panel b.

3.3. Two days after a storm

Figure 5 shows a 1.8-Hz hydrogen band wave event with peak amplitude of 0.8 nT observed from 06:30 to ~07:10 UT during an outbound pass near 10:00 MLT on March 2, 2014, two days after the end of the main phase of a magnetic storm with minimum Dst = -94. During this event AE ~ 30 nT, after a peak at 150 nT at 0500 UT, and Dst = -23. The event coincided with a slight increase in solar wind pressure in otherwise steady geomagnetic conditions. Two slots are evident in the ring current fluxes, with deep minima near ~8 and ~40 keV (panel d). Proton fluxes at energies between these slots were moderately anisotropic near 20 keV and strongly anisotropic near 50 keV; fluxes at these energies increased sharply shortly before the onset of the wave event. MagEIS fluxes at all available energies were also anisotropic, and decreased steadily with time from energy-dependent peaks beginning at the highest energies before 06:00 UT (panel c). Peak fluxes in the lowest energy range (58 keV) coincided with the duration of the wave event, and fluxes in the next lowest range reached their maximum at the time of wave onset; all others had peak values well before wave onset and decreased steadily throughout the wave event.

Figure 6 shows a ~2.2 Hz H-band wave event with peak amplitude of 0.8 nT that occurred outside a plasmaspheric plume from 07:22 to 07:48 UT, with L from 4.4 to 4.9, during

an outbound pass near 09:00 MLT on April 14, 2014, two days after the main phase of a magnetic storm with minimum Dst = -81. The AE index rose to \sim 500 at 06:20 UT, but during the wave event AE \sim 300 nT, while Dst remained steady at -19. Warm protons and plasma sheet ions (\sim 5 eV to \sim 500 eV) extended inward to L \sim 3.2 (panel d), while more energetic ring current ions extended inward to below L \sim 2 (panel c). A deep minimum separated enhanced fluxes of protons above 20 keV from protons below \sim 8 keV during the wave event (panel d). Fluxes of anisotropic protons with energies above 40 keV (panel d) and from 50 to 130 keV (panel c) increased gradually from \sim 07:10 UT to 07:45, coincident with the duration of the wave event.

Figure 7 shows a He-band 0.6-Hz wave event with peak amplitude of 2.6 nT that was observed from 16:50 to 17:10 UT during an inbound crossing of the inner edge of the plasmapause at L=4.8 near local noon on May 10, 2014, two days after the main phase of a magnetic storm with minimum Dst = -44. The AE index rose to ~500 nT near 04:00 UT on this day, but remained steady below 100 nT from 10:00 until 18:00 UT, and Dst was near -15 nT over this same time interval. The spurious constant tones near 0.1, 0,19, 0.38, and 0.57 Hz are subharmonics and aliased tones from the ~1.4 Hz heater signal.

This wave event coincided with a sharp plasmapause (panel b) and with the inner boundary of the cool 1-10 eV plasma evident at the bottom of panel d, as well as an approximate inner boundary of plasma sheet ions (10 eV - 2 keV). Ring current protons exhibited a slot near 20 keV, with 8 to 20 keV ring current protons extending inward from this boundary to L \sim 3.6 (panel d). More energetic ring current ions (panel c) extended farther inward (down to L \sim 2.2 at energies \geq 100 keV), but fluxes at energies from 80 to 100 keV peaked in the 16:50 to 17:50 time range. The flux at 58 keV peaked at the time of the wave event, from 16:50 to 17:10, and largest fluxes were in this channel (not shown).

3.4. Generalizations from these examples

In each of the seven examples shown above, EMIC events were associated with increased fluxes of ring current ions. The energy of the ions most closely associated in time with the wave event varied considerably, from ~20 keV to over 100 keV. In some but not all cases, the waves were also associated with regions of increased densities of cold ions or the boundaries of such regions. We note also that the inward extent of ≤ 50 keV ring current ions was often associated with a plasma density gradient, but the inward extent of ≥ 100 kev ions was rarely if ever bounded by such gradients. This is consistent with recent observations by Zhao et al. [2015] and Gkioulidou et al. [2016] showing that peak ring current fluxes of the more energetic ring current ions (≥ 100 keV) were frequently observed at considerably lower L shells than those of the lower energy ring current ions.

4. Statistical Study

4.1 Distribution of EMIC events in ΔL relative to the PP

EMIC wave generation has previously been thought to occur in areas where field strength is low or the plasma mass density is high [Cornwall, 1965, 1966; Kennel and Petschek, 1966, Chen et al., 2009]. Because of these dependences, both the plasmapause and plumes (regions of high density at L shells beyond the plasmapause) have been considered to be preferred regions for wave growth. Complex electrodynamic interactions determine the location of the plasmapause and the possible stripping off of high-density regions to form plumes, and the example events shown in Figures 1-7 reveal both the variability and complexity of such profiles. These examples demonstrate that the location of unstable ring current ions is a necessary condition for EMIC wave generation; in some but not all cases these waves are also associated

with regions of high density. In this section, however, we ignore the complexities of such high-density regions, and focus on the 55 of 78 events for which there were clear plasmapause structures, with significantly higher densities inside the PP than outside. We categorized events using bins of 0.1 L relative to the observed PP, and of one hour of magnetic local time (MLT). Individual events often spread over several bins.

Figure 8 presents the distributions of EMIC waves relative to the observed PP in four local time quadrants. Most EMIC waves occurred within 1 R_E of the PP, but very few were limited to \pm 0.1 R_E . Events that went beyond 1 R_E outside the PP were common in the dayside sectors (06 – 18 h MLT, panels c and d), indicative of events stimulated by solar wind compressions or (in a few cases) associated with plasmaspheric plumes. The events that were inside the PP were proportionally most common in the 12 – 24 h MLT sectors (panels d and e)

. These results are consistent with the study by Anderson et al., [1992a] that found occurrence rates for EMIC waves at L values above 8 (outside the PP) to be low from 19:00 – 03:00 MLT.

4.2 Distribution as a function of frequency band relative to the PP

Figure 9 shows histograms of EMIC wave occurrences as a function of local time quadrant and frequency band (hydrogen (H), helium (He), or both – waves occur in both bands), separated into events inside, at, or outside the PP, or "other", which includes complex density structures, plumes, and passes with no sharp PP density gradient, out to the Van Allen Probe A apogee near L = 5.9. Figure 9 shows that H-band EMIC waves constituted nearly all of the events at the PP in the 06 - 12 h MLT sector, and most of the events outside the PP in all local time sectors, but H-band events were never observed inside the PP. This peak in H-band EMIC

wave events around the pre-noon MLT sector has only been observed in the recent Saikin et al. [2016] study, while earlier studies had a mainly dawn-centered hydrogen-band peak at high L shells [Min et al., 2012; Usanova et al., 2012]. Events with power in both the H- and He-bands were often observed inside the PP in the 06 – 18 h MLT sectors, but were not observed at other local times. This local time peak of events is consistent with the observations of Saikin et al. [2015] and studies that reported dominant EMIC wave source regions in the afternoon sector due to the overlap with H- and He-band peaks [Jordanova et al., 2001, 2008]. He-band EMIC wave events dominated over most local times inside the PP, and occurred often at the PP over a wide range of local times. These results are consistent with those of Saikin et al. [2015] who observed He-band EMIC wave events at all MLT. The locations of H- and He- band waves relative to the PP observed in this study are also in agreement with Figure 13 of Fraser and Nguyen [2001], showing that H-band events were observed only at and outside the PP while He-band events were observed outside, at, and inside the PP.

4.3 Distribution of EMIC waves in relation to MLT and ΔL relative to the PP – sorted by storm phase

Figure 10 shows the distribution of EMIC waves as a function of MLT (vertical axis) and Δ L from the observed PP (horizontal axis), color-coded by storm phase. We also sorted these events by frequency band: hydrogen, helium, or both (Figure 11). There was only one pre-onset phase event, which occurred at 03:00 MLT at the location of the PP. Main phase events occurred between 16:00 and 03:00 MLT, and most of these occurred at or just inside the PP, meaning the majority of the wave was at the PP but some portion was inside. Recovery phase events occurred over a wide range of MLT and Δ L, most of which were not located at the PP

boundary. Quiet and compressional events occurred at all local times and with wide variations in ΔL, but occurred mainly between 08:00 and 13:00 MLT, and only rarely coincided with the PP. This local time range is consistent with the observations of Park et al. [2016] at geosynchronous orbit that quiet time EMIC waves (including those during isolated compressions) mostly occurred on the dayside with a peak occurrence near noon. Panel a of Figure 11 shows that helium-band events occurred at all local times, while hydrogen-band events (panel b) were more common during pre-noon local times and events appearing simultaneously in both bands (panel c) were limited to near-dusk and post-midnight local times. As Table 1 shows, the majority of the events were in the recovery and quiet phases, consistent with results of the Saikin et al. [2016] study.

5. Superposed Epoch Analysis

In this section we present three sets of superposed epoch plots that focus on some of the conditions favorable for the occurrence of EMIC waves: nightside auroral activity / substorms, magnetic storms, and increases in solar wind dynamic pressure. Plots are presented for wave events outside, at, and inside the PP (Figure 12), in four local time sectors (0-6, 6-12, 12-18, and 18-24 h MLT, Figure 13), and during four magnetic storm phases (compressions, main phase, recovery phase, and quiet intervals, Figure 14), using definitions presented by Halford et al. [2010] and also used in statistical studies of Van Allen Probe data by Saikin et al. [2015, 2016]. All 78 wave events were used in the MLT and storm phase plots, but only the 55 events during which a clear PP could be identified within two hours of the wave event were used for the plots relative to PP location.

Also shown in each of these figures are plots using the 1-hour Dst index, commonly used to quantify the strength of magnetic storms and identify storm phases, and the solar wind pressure Psw and its variation over 5 minutes (ΔPsw), both using data from the OMNI database (http://cdaweb.gsfc.nasa.gov). In each figure the mean, 75th percentile, and 25th percentile values of these quantities were calculated during 27 hourly intervals, from 0 up to 24 hours prior to the onset of an EMIC wave event, and up to 3 hours after wave onset.

5.1 EMIC waves by location relative to the PP

Figure 12 presents the results from superposed epoch analyses of the SME and Dst indices, solar wind dynamic pressure (Psw), and 5-min variations in Psw (ΔPsw) during, before, and 3 hours after EMIC wave events relative to the location of the observed PP, but summed over all storm phases and local time sectors.

EMIC wave events outside the PP were preceded by a gradual drop of ~100 nT in the mean SME index (panel a) during the 24 hours prior to onset, a modest rise of 50 nT one hour before onset, and a gradual drop of ~40 nT during the following 3 hours. All three traces showed considerable variability in the first 22 hours shown (especially the top trace), an increase 1 hour before onset, and a slight drop to lower values during the following 3 hours.

For events at the PP (panel b) the mean SME index showed a gradual ~100 nT rise during the first 24 hours, a modest 50 nT rise one hour before onset, followed by an immediate drop of 30 nT. Again all three traces showed roughly similar behavior, but with more variability in the 75th percentile trace. For events inside the PP (panel c), all traces showed larger increases during the first 24 hours and peaks 1-2 h before onset, followed by a post-onset decrease. The mean SME index more than doubled from epoch -24 h to -1 h, increasing by 300 nT, and then

dropping by ~200 nT during the next 3 h. Panels a,b, and c all show a close temporal correlation between EMIC wave onset and increases in SME within the prior 1-2 hours; the amplitude of this increase was, however, much larger for events inside the PP. The time history of the SME index from -24 to -2 h also exhibited different trends for events outside, at, and inside the PP: for events outside the PP (panel a) SME declined from nearly 500 nT to ~300 nT, while for events at the PP (panel b) SME rose from ~ 300 to ~450 and for events inside the PP (panel c) SME remained < 300 nT until -6 h.

The mean Dst index trace in panels d,e,f in Figure 12 showed much less variation than the mean SME trace, even though both the 75th and 25th percentile traces showed large and seemingly unrelated variations during the first 24 hours. Wave onset outside (panel d) and at (panel e) the PP coincided with a slight (~5 nT) rise in mean Dst as well as modest increases in the 75th and 25th percentile traces, while onset inside the PP occurred during the middle of a 6-hour 15-nT decrease in mean and 75th percentile Dst and a modest rise in 25th percentile Dst.

Panels g and i of Figure 12 show that rapid increases in Psw occurred before EMIC wave onset both outside and inside the PP boundary. For events outside the PP (panel g) Psw increased rapidly from about 3 to 4 nPa 1 to 2 hours before onset, and peaked at the time of onset. Events inside the PP (panel i) showed similar variations. Psw increased prior to the event, with the greatest increase about 2 hours before the onset, again reaching a maximum mean value of about 4 nPa. In contrast, the mean Psw for events that occurred at the PP location (panel h) tended to stay constant throughout all hours prior to the event, and exhibited only a <1 nPa rise shortly before and during the event. EMIC wave events that occurred outside or inside the PP were clearly associated with increased Psw, while events that occurred at the PP location showed

only a slight dependence on Psw. The lower traces in both panels g and i, however, showed very little change in Psw for several hours before, during, and after wave onset, indicating that some events occurred during intervals of steady Psw. Park et al. [2016] found a similar pattern in their study of EMIC waves observed during geomagnetically quiet conditions at geosynchronous orbit: the mean and 75th percentile values of Psw increased shortly before wave onset, but not the 25th percentile values.

Although increases in Psw are known to be one factor contributing to increases in Dst, only in panel g (i.e., outside the PP) did the mean Dst and Psw traces both show an increase from -24 h to 0 h.

We also investigated the effect of short-term (5-minute) changes in Psw (Δ Psw), independent of their prior level, in an attempt to investigate whether such short-term changes influenced wave generation independently of the pressure level. One-h averages of the mean Δ Psw (panels j,k,l) remained consistently below ± 0.1 nPa per 5 min, but showed more variability beginning ~4 h before wave onset. However, the 75th and 25th percentile traces showed somewhat different behavior in the three regions. Both positive and negative variations in Psw peaked 1 h before onset for waves outside the PP (panel j) and remained at elevated levels (up to ± 1 nPa per 5 min) during the next 3 h. From 24 to 15 hours before the onset of wave activity inside the PP (panel l), the 75th and 25th percentile traces were mostly below ± 0.2 nPa. Both traces showed larger increases in magnitude 6 h before onset, and returned to lower values 2-3 h afterward. However, these same traces were relatively steady and with magnitude > 0.3 nPa during the entire 27-h interval for events at the PP (panel k), showing little evidence of change at the time of wave onset.

The slightly weaker variations in all four panels of Figure 12 immediately before and during events at the PP (panels b, e, h, and k) suggest that events at the PP might be attributed to some spatial factor (such as a plasmapause gradient). In order to investigate this further, we performed the same analyses for events in the H and He bands, and in both bands separately (8, 10, and 2 events, respectively, as shown in row 2 of Figure 9). The resulting plots (not shown) indicated that within 3 h of onset SME dropped slightly (< 50 nT) for H band events but rose by >200 nT for He band events and ~100 nT for the two H-He band events. Conversely, within 2 h of onset Psw rose by 1.5 nPa for H band events but remained constant to within 0.2 nPa for He and H-He band events, and Dst rose by < 10 nT within 2 h of onset for H band events, but remained nearly constant for He and H-He band events. The superposed epoch patterns for H band events at the PP thus closely resemble those for events outside the PP (dominated by H band events, as shown in row 3 of Figure 9) in being associated with increased Psw, while the patterns for He and H-He band events at the PP resemble those for events inside the PP (dominated by He band events and events in both H and He bands, as shown in row 1 of Figure 9), in being associated with increased SME. There is thus no evidence in this superposed epoch analysis to suggest any spatial factors associated with the PP that might increase the probability of wave onset. We point out, however, that although a superposed epoch analysis shows only temporal variations, spatial and temporal variations simply cannot be separated using data from a single elliptically-orbiting spacecraft. We intend to pursue this issue further in a subsequent study using observations of EMIC waves observed by both Van Allen Probes spacecraft, which because of their slightly different orbits pass a given location with a range of delay times from a few min to several hours.

5.2 EMIC waves by MLT sector

520

521

522

523

524

525

526

527

528

529

530

531

532

533

534

535

536

537

538

539

540

541

542

A similar analysis using the SME and Dst indices, Psw, and ΔPsw was performed for all 78 EMIC wave events sorted by four magnetic local time sectors (00 – 06 h, 06 – 12 h, 12 – 18 h, and 18 – 24 h MLT). In the 0-6 h and 6-12 h MLT sectors there was little change in the SME index (panels a,b), and only a slight rise in Dst about 2 hours before the EMIC wave events (panels e,f). In contrast, panels i and j each showed gradual increases in Psw for several hours before onset and more rapid increases in Psw just before onset. This comparison suggests that wave onset in these sectors was dominated or triggered by compressions.

In both the 12 – 18 h and 18 – 24 h sectors, in contrast, SME rose substantially before onset (panels c,d), and Dst fell slightly (panels g,h). Although Psw also increased shortly before onset in the 12-18 h sector (panel k), it was nearly constant for several hours before and during onset in the 18-24 h sector (panel l). In both of these local time sectors the mean SME index increased by over 200 nT before onset, but its increase occurred later and more rapidly in the 18 – 24 h sector than in the 12-18 h sector. This temporal pattern is consistent with that reported by Saikin et al. [2016], who observed that the AE index increased as peak occurrence of EMIC waves shifted from the pre-noon sector to the dayside.

Although there was a clear rise in Psw before onset in all but the premidnight (18-24 h) sector, it is notable that the mean Psw peak and the 75th percentile peak at onset in the 0-6 h sector (panel i) were larger than those in the two dayside sectors (6-12 and 12-18 h, panels j and k). Although this may appear counterintuitive (increases in Psw would most strongly compress the magnetosphere on the day side, and thus increase the temperature anisotropy of ring current protons), evidence from several observational studies suggests that dynamical effects in the postmidnight sector can also cause significant responses to solar wind pressure increases

including subauroral proton auroras, presumably caused by EMIC waves (Meurant et al. [2003]; Lee et al. [2005, 2007]; Zhang et al. [2005, 2008]; and Søraas et al. [2013]).

Panels m,n,o, and p of Figure 13 again show that throughout all MLT sectors the mean ΔPsw tended to stay consistently near zero. Both the upper (75th) and lower (25th) percentile delta solar wind values in each local time quadrant also showed increasingly large deviations from 0, but these were again significantly larger in the 0-6 h quadrant.

5.3 EMIC waves by storm phase

Figure 14 shows the results of applying the same superposed epoch analysis after sorting the 78 events according to storm phase (Figure 14). The one Pre-Onset event listed in Table 1 was included in the Compressional events category for this analysis. During compressions, the SME index remained relatively constant (panel a), whereas the Dst index gradually increased beginning ~24 hours prior to wave onset (panel e). The mean Psw value began a large, steady increase beginning about 6 h prior to onset that continued until 1 h after onset (2 to 7 nPa, panel i). Although the mean ΔPsw traces remained near 0 during each storm phase (panels m, n, o, and p), the increase in Psw during compressions was reflected in the large 75th percentile ΔPsw trace before onset, and the moderate drop in Psw after onset was reflected in a large negative 25th percentile ΔPsw trace during that interval (panel m).

Main phase EMIC wave events were associated with a nearly step-like increase in SME roughly 12 hours before onset as well as a large, steady increase during the 5 hours prior to onset, reaching a mean peak of 850 nT (panel b). During main phase Dst exhibited a monotonic decrease throughout the 27-hour interval shown, from 0 to \sim -60 nT (panel f). Main phase events

also showed a gradual increase in Psw (with peak level over 4 nPa at onset, panel j), and with relatively large values of 75th and 25th percentile traces in ΔPsw (panel n).

Recovery phase events showed a rise and subsequent fall in SME from -24 h to -2 h, but a small rise 1 h prior to onset and a peak at the time of the event (panel c), and a slight fall and subsequent rise in Dst from -24 h to -2 h, followed by a somewhat more rapid rise during and after onset (panel g). The mean SME index during the quiet phase was relatively constant except for a small ~50-nT rise 1-2 hours before onset (Panel d), and Dst was relatively constant through the interval shown (panel h). Mean Psw values showed only modest changes during both the recovery and quiet phases (panels k,l), but were ~1 nPa higher during the former. The 75th and 25th percentile traces in ΔPsw were elevated during all 27 h for events during the recovery phase (panel o), but remained at lower levels during all 27 h for events during the quiet phase (panel p).

6. RMS amplitudes of EMIC waves

The root mean square (RMS) amplitude of the transverse component of each EMIC wave event was calculated using the Gaussfit function in IDL. The amplitude values were tabulated and placed into color-coded amplitude ranges to then analyze the distribution as a function of MLT and ΔL (Figure 15). The one EMIC wave event with RMS amplitude < 0.3 nT was located at 10:00 MLT outside the PP boundary. Events with values between 0.3 – 1.0 nT were observed over all local times, mainly outside the PP. Events with 1.0 – 3.0 nT amplitude were also seen throughout all local times, but mainly located inside the PP. Wave events with RMS amplitude values between 3.0 – 10.0 nT were also widely distributed across MLT sectors and seen outside, at, and inside the PP boundary. Events with the largest RMS amplitude values (> 10.0 nT) were only observed at 22:00 MLT, at the PP boundary, and 00:00 MLT, outside the PP.

These RMS amplitude plots were also separated by frequency bands (Figure 16). The majority of EMIC wave events with RMS amplitudes between 0.3 and 1.0 nT occurred in the hydrogen band, although they were observed in the helium band as well. The majority of the events with amplitudes between 1.0 and 3.0 nT were observed in the helium band, but also seen in the hydrogen band. The events with the largest RMS amplitude values (> 10.0 nT) were seen in both hydrogen and helium bands at 00:00 and 22:00 MLT, respectively.

7. Discussion and Conclusion

This study has documented the location, relative to the plasmapause, of the most intense EMIC waves observed during the first 27 months of the Van Allen Probes A mission. Figure 8 shows that intense waves occurred over a moderate range of ΔL (+2 / -1 R_E) from the PP in all local time sectors. Occurrence in each sector was largest within 0.2 R_E of the PP, but was peaked to within \pm 0.05 R_E of the PP only in the 06 – 12 h MLT sector. Figure 10, which shows individual events plotted as a function of local time as well as ΔL , makes it clear that very few events occurred only within 0.1 R_E of the PP, and that events similarly narrow in L, or even narrower, occurred at locations both inside and outside the PP. This lack of close spatial alignment of wave events with the PP is consistent with a theoretical study by Denton et al. [2014] that found little support for the importance of a sharp density gradient in generating EMIC waves, and with a superposed epoch study by Halford et al. [2015] that found no correlation between the occurrence of EMIC waves and a negative density gradient in the 14-18 h MLT range during both the main phase of geomagnetic storms and during all storm or nonstorm phases. However, even though the PP is not the dominant factor in EMIC wave

generation, it does seem to be an approximate organizing factor during all magnetic storm phases and in all local time sectors.

629

630

631

632

633

634

635

636

637

638

639

640

641

642

643

644

645

646

647

648

649

650

651

Using seven examples (Section 3), we identified patterns within the ion populations associated with EMIC wave events. As has been found in many other studies, the conditions for EMIC wave occurrence required sufficiently high densities of ring current ions, and often (but not always) these waves were also associated with increased densities of either or both warm (plasma sheet) ions and thermal (cold) ions. Waves occurred during all phases of magnetic storms, and their locations depended on the complex interplay between different ion populations.

The intense EMIC waves identified in this study occurred mainly in the recovery and quiet phases of geomagnetic storms (Table 1), consistent with the Saikin et al. [2016] study. We found that main and recovery phase EMIC waves in the dusk sector were often inside the PP (Figure 10), and as shown in the example events, ring current fluxes (especially at higher energies) were at times observed well inside the PP in various local time sectors. Although the inner radial extent to which lower energy ($\leq 80 \text{ keV}$) ring current ions can penetrate during and after injections is subject to a complex set of factors including increased dawn-dusk electric fields, gradient-curvature drifts, and ExB drifts (discussed for example in Thaller et al. [2015]), both ring current injections and the quiet-time plasmaspheric bulge occur in the dusk sector, so this region is the easiest place for the lower energy ring current and cold plasma to overlap under active conditions, consistent with the observations shown in Figures 9 and 10. Subsequently, when the convection electric field turns off, the ion drift should become symmetric, and the bulge regions of the plasmasphere should begin to rotate. Hence in the early recovery phase the region of hot ion / cold plasma overlap could vary in MLT with a 24-hour period. The different dynamics of lower and higher energy ring current populations recently documented by Zhao et

al. [2015] and Gkioulidou et al. [2016] also appear to play a role here: in several examples EMIC waves were observed in regions with increased densities of ≥ 100 keV ions.

Superposed epoch analyses (Figures 12-14) showed that EMIC wave events were temporally related to changes in the SME and Dst indices and to solar wind dynamic pressure (Psw) and its variations in ways that depended on location relative to the PP, local time, and geomagnetic storm phase. We note that Figures 2-4 of Halford et al. [2016] have documented a very complex relationship between the occurrence of EMIC waves in the CRRES data set and the actual levels of AE, Sym-H, and Kp, and concluded that these indices are not good proxies for EMIC wave activity. Figures 12-14 show that short-term (few-hour) changes in one or more of SME, Dst, and Psw are well correlated with EMIC onsets when events are broken down by MLT, ΔL, and storm phase, but, consistent with the conclusion of Halford et al. [2016], their levels are not.

Large increases in Psw were associated with EMIC waves in the post-midnight (00 - 06) MLT sector, and also exhibited a slight rise before onsets on the dayside (06 - 18 h MLT), while pre-midnight (18 - 24 h) MLT sector events had little to no dependence on solar wind dynamic pressure. EMIC wave events during the compression, main, and recovery phases of geomagnetic storms were also found to be temporally associated with rising Psw values. Increases in Psw were associated with EMIC wave events located both inside and outside the observed PP location, as well as with H band (but not He band) events at the PP.

We also analyzed the impact of the SME and Dst indices on EMIC wave generation. We found that waves in the 00 - 12 h MLT sectors were dominated by compressions (a rise in Dst), while waves in the 12 - 24 h MLT sectors were related to magnetic disturbances (a rise in SME).

EMIC wave events inside the PP, as well as He band events at the PP, were found to be preceded by significant increases in SME. Compressional phase EMIC wave events were on average preceded by a slight increase in Dst, with no clear change in SME index, while both main and quiet phase events were preceded by an increase in SME and a decrease in Dst. In contrast, recovery phase events were preceded by an overall decrease in SME and a clear increase in Dst, but these events also showed a small rise in SME shortly before wave onset.

This study has thus shown that EMIC waves are approximately but not closely linked to the PP position. We found, through the use of HOPE and MagEIS ring current data, that wave occurrence was always associated with high densities of ring current ions, and that plasma density gradients or enhancements may have contributed to wave occurrence but were not the dominant factor in determining the sites of wave generation. This study also analyzed the RMS amplitudes for each wave event, showing that large amplitude waves in the Van Allen Probes data set were distributed across all MLT sectors and occurred outside, at, and inside the PP. It also has shown that substorm injections and solar wind compressions were temporally closely associated with EMIC wave onset, but to an extent that varied with location both in MLT and relative to the PP and with storm phase.

Acknowledgements

Work at Augsburg College was supported by NSF grants PLR-1341493 and ATM-1202267 to Augsburg College, and work performed by M.J.E. at NASA/GSFC was supported by the Van Allen Probes mission. Van Allen Probes research at the University of Minnesota, University of Iowa, University of New Hampshire, Los Alamos National Laboratory, and the Aerospace

696	Corporation was supported by NASA prime contract NAS5-01072 to The Johns Hopkins
697	University Applied Physics Laboratory. We thank David Sibeck, Brian Anderson, and
698	Viacheslav Pilipenko for helpful comments. We gratefully acknowledge use of NASA/GSFC's
699	Space Physics Data Facility's OMNIWeb, SSCweb, and CDAWeb data. Van Allen Probes CDF
700	data files are available at http://rbsp.space.umn.edu/rbspdata/ (EFW) and
701	http://emfisis.physics.uiowa.edu/dta/index (EMFISIS). Plots of HOPE and MagEIS data are
702	available from the CDAWEB site at NASA Goddard Space Flight Laboratory
703	(<u>http://cdaweb.gsfc.nasa.gov/</u>). For the ground magnetometer data we gratefully acknowledge:
704	Intermagnet; USGS, Jeffrey J. Love; CARISMA, PI Ian Mann; CANMOS; The S-RAMP
705	Database, PI K. Yumoto and Dr. K. Shiokawa; The SPIDR database; AARI, PI Oleg Troshichev
706	The MACCS program, PI M. Engebretson, Geomagnetism Unit of the Geological Survey of
707	Canada; GIMA; MEASURE, UCLA IGPP and Florida Institute of Technology; SAMBA, PI
708	Eftyhia Zesta; 210 Chain, PI K. Yumoto; SAMNET, PI Farideh Honary; The institutes who
709	maintain the IMAGE magnetometer array, PI Eija Tanskanen; PENGUIN; AUTUMN, PI Martin
710	Connors; DTU Space, PI Dr. Rico Behlke; South Pole and McMurdo Magnetometer, PI's Louis
711	J. Lanzarotti and Alan T. Weatherwax; ICESTAR; RAPIDMAG; PENGUIn; British Antarctic
712	Survey; McMac, PI Dr. Peter Chi; BGS, PI Dr. Susan Macmillan; Pushkov Institute of
713	Terrestrial Magnetism, Ionosphere and Radio Wave Propagation (IZMIRAN); GFZ, PI Dr.
714	Juergen Matzka; MFGI, PI B. Heilig; IGFPAS, PI J. Reda; University of L'Aquila, PI M.
715	Vellante; SuperMAG, PI Jesper W. Gjerloev.
716	
717	

719 References

- Anderson, B. J., Erlandson, R. E., Zanetti, L. J. (1992a), A statistical study of Pc 1-2 magnetic
- 721 pulsations in the equatorial magnetosphere 1. Equatorial occurrence distributions, J. Geophys.
- 722 Res., 97, 3075.
- Anderson, B. J., Erlandson, R. E., Zanetti, L. J. (1992b), A statistical study of Pc 1-2 magnetic
- pulsations in the equatorial magnetosphere 2. Wave properties, *J. Geophys. Res.*, 97, 3089.
- Anderson, B.J., and D. G. Hamilton (1993), Electromagnetic ion cyclotron waves stimulated by
- modest magnetospheric compressions, *J. Geophys. Res.*, 98, 11,369-11,382.
- Arnoldy, R. L., M. J. Engebretson, R. E. Denton, J. L. Posch, M. R. Lessard, N. C. Maynard, D.
- M. Ober, C. J. Farrugia, C. T. Russell, J. D. Scudder, R. B. Torbert, S.-H. Chen, and T. E. Moore
- 729 (2005), Pc 1 waves and associated unstable distributions of magnetospheric protons observed
- during a solar wind pressure pulse, J. Geophys. Res. Sp. Phys., 110, A07,229,
- 731 doi:10.1029/2005JA011041.
- Blake, J. B. et al. (2013), The magnetic electron ion spectrum-eter (MagEIS) instruments aboard
- the radiation belt storm probes (RBSP) spacecraft. Space Sci. Rev., 179:383-421,
- 734 doi:10.1007/s11214-013-9991-8.
- 735 Campbell, W. H. (1967), Low attenuation of hydromagnetic waves in the ionosphere and implied
- characteristics in the magnetosphere for Pc1 events, *J. Geophys. Res.*, 72, 3429 3345.
- 737 Chen, L., R. M. Thorne, and R. B. Horne (2009), Simulation of EMIC wave excitation in a
- model magnetosphere including structured high-density plumes, J. Geophys. Res., 114, A07221,
- 739 doi:10.1029/2009JA014204.

- 740 Cornwall, J. M. (1965), Cyclotron instabilities and electromagnetic emission in the ultra low
- frequency and very low frequency ranges, *J. Geophys. Res.*, 70, 61.
- Cornwall, J. M. (1966), Micropulsations and the outer radiation zone, J. Geophys. Res., 71, 2185.
- Cornwall, J. M., Coroniti, F. V., Thorne, R. M. (1970), Turbulent loss of ring current protons, J.
- 744 Geophys. Res., 75, 4699.
- Denton, R. E., V. K. Jordanova, and B. J. Fraser (2014), Effect of spatial density variation and
- O⁺ concentration on the growth and evolution of electromagnetic ion cyclotron waves, J.
- 747 Geophys. Res. Space Physics, 119, 8372–8395, doi:10.1002/2014JA020384.
- Engebretson, M. J., W. K. Peterson, J. L. Posch, M. R. Klatt, B. J. Anderson, C. T. Russell, H. J.
- Singer, R. L. Arnoldy, and H. Fukunishi (2002), Observations of two types of Pc 1-2 pulsations
- in the outer dayside magnetosphere, J. Geophys. Res., 107(A12), 1451,
- 751 doi:10.1029/2001JA000198.
- 752 Engebretson, M. J., et al. (2008a), Pc1 Pc2 waves and energetic particle precipitation during
- and after magnetic storms: Superposed epoch analysis and case studies, J. Geophys. Res., 113,
- 754 A01211, doi:10.1029/2007JA012362.
- Engebretson, M. J., et al. (2008b), Temporal and spatial characteristics of Pc1 waves observed by
- 756 ST5, J. Geophys. Res., 106(A3), 3883 3895, doi:10.1029/2008JA013145.
- 757 Engebretson, M. J., J. L. Posch, J. R. Wygant, C. A. Kletzing, M. R. Lessard, C.-L. Huang, H. E.
- 758 Spence, C. W. Smith, H. J. Singer, Y. Omura, R. B. Horne, G. D. Reeves, D. N. Baker, M.
- 759 Gkioulidou, K. Oksavik, I. R. Mann, T. Raita, and K. Shiokawa (2015), Van Allen probes,

- NOAA, GOES, and ground observations of an intense EMIC wave event extending over 12 h in
- magnetic local time, J. Geophys. Res. Space Physics, 120, doi:10.1002/2015JA021227.
- Francisco, R. E., and A. J. Ukhorskiy (2001), Observations of electromagnetic ion cyclotron
- 763 waves during geomagnetic storms: Wave occurrence and pitch angle scattering, *J. Geophys.*
- 764 Res., 106(A3), 3883 3895, doi:10.1029/2000JA000083.
- Fraser, B. J., and T. S. Nguyen (2001), Is the plasmapause preferred source region of
- electromagnetic ion cyclotron waves in the magnetosphere?, J. Atmos. Sol. Terr. Phys., 63, 1225
- 767 1247, doi:10.1016/S1364-6826(00)00225-X.
- Fraser, B. J., R. S. Grew, S. K. Morley, J. C. Green, H. J. Singer, T. M. Loto'aniu, and M. F.
- 769 Thomsen (2010), Storm time observations of electromagnetic ion cyclotron waves at
- geosynchronous orbit: GOES results, *J. Geophys. Res.*, 115, A05208,
- 771 doi:10.1029/2009JA014516.
- Funsten, H. O. et al. (2013), Helium, Oxygen, Proton, and Electron (HOPE) instruments aboard
- the radiation belt storm probes (RBSP) spacecraft, Space Sci. Rev., 179, 423 484,
- 774 doi:10.1007/s1124-013-9968-7.
- 775 Gkioulidou, M., A. Y. Ukhorskiy, D. G. Mitchell, and L. J. Lanzerotti (2016), Storm time
- dynamics of ring current protons: Implications for the long-term energy budget in the inner
- magnetosphere, *Geophys. Res. Lett.*, 43, 4736-4744, doi:10.1002/2016GL068013.

- Halford, A. J., B. J. Fraser, and S. K. Morley (2010), EMIC wave activity during geomagnetic
- storm and nonstorm periods: CRRES results, J. Geophys. Res. Sp. Phys., 115, 1-15,
- 781 doi:10.1029/2010JA015716.
- Halford, A. J., B. J. Fraser, and S. K. Morley (2015), EMIC waves and plasmaspheric and
- 783 plumedensity: CRRES results, J. Geophys. Res. Space Physics, 120, 1974–1992,
- 784 doi:10.1002/2014JA020338.
- Halford, A. J., B. J. Fraser, S. K. Morley, S. R. Elkington, and A. A. Chan (2016), Dependence
- of EMIC wave parameters during quiet, geomagnetic storm, and geomagnetic storm phase times,
- 787 *J. Geophys. Res. Space Physics*, 121, doi:10.1002/2016JA022694.
- Heacock, R. R., and M. Kivinen (1972), Relation of Pc1 micropulsations to the ring current and
- 789 geomagnetic storms, *J. Geophys. Res.*, 77, 6746 6760.
- Jordanova, V. K., C. J. Farrugia, R. M. Thorne, G. V. Khazanov, G. D. Reeves, and M. F.
- 791 Thomsen (2001), Modeling ring current proton precipitation by electromagnetic ion cyclotron
- 792 waves during the May 14 16, 1997, storm, *J. Geophys. Res.*, 106, 7 22,
- 793 doi:10.1029/2000JA002008.
- Kaye, S. M., and M. G. Kivelson (1979), Observations of Pc 1 -2 waves in the outer
- 795 magnetosphere, *J. Geophys. Res.*, 84, 4267 4276.
- Keika, K., K. Takahashi, A. Y. Ukhorskiy, and Y. Miyoshi (2013), Global characteristics of
- 797 electromagnetic ion cyclotron waves: Occurrence rate and its storm dependence, J. Geophys.
- 798 Res. Sp. Phys., 118, 4135 4150, doi:10.1002/jgra.50385.

- Kennel, C. F., and H. E. Petschek (1966), Limit on stably trapped particle fluxes, J. Geophys.
- 800 *Res.*,71, 1.
- Kletzing, C. A., et al. (2013), The Electric and Magnetic Field Instrument Suite and Integrated
- 802 Science (EMFISIS) on RBSP, Space Sci. Rev., 179, 127 181, doi:10.1007/s11214-013-9993-6.
- Kozyra, J. U., T. E. Cravens, F. Nagy, and E. G. Fontheim (1984), Effects of energetic heavy
- ions on electromagnetic ion cyclotron wave generation in the plasmapause region, *J. Geophys.*
- 805 *Res.*, 89(A4), 2217 2233, doi:10.1029/JA089iA04p02217.
- Lee, D.-Y., L. R. Lyons, and G. D. Reeves (2005), comparison of geosynchronous energetic
- particle flux responses to solar wind dynamic pressure enhancements and substorms, *J. Geophys.*
- 808 Res., 110, A09213, doi:10.1029/2005JA011091.
- Lee, D.-Y., S. Ohtani, P. C. Brandt, and L. R. Lyons (2007), Energetic neutral atom response to
- solar wind dynamic pressure enhancements, J. Geophys. Res., 112, A09210,
- 811 doi:10.1029/2007JA012399.
- Lyons, L. R., R. M. Thorne, and C. F. Kennel (1972), Pitch-angle diffusion of radiation belt
- electrons within the plasmasphere, *J. Geophys. Res.*, 77, 3455 3474,
- 814 doi:10.1029/JA077i019p03455.
- McCollough, J. P., S. R. Elkington, M. E. Usanova, I. R. Mann, D. N. Baker, and Z. C. Kale
- 816 (2010), Physical mechanisms of compressional EMIC wave growth, J. Geophys. Res., 115,
- 817 A10214, doi:10.1029/2010JA015393.

- McCollough, J. P., S. R. Elkington, and D. N. Baker (2012), The role of Shabansky orbits in
- compression-related electromagnetic ion cyclotron wave growth, J. Geophys. Res., 117, A01208,
- 820 doi:10.1029/2011JA016948.
- Merka, J., A. Szabo, J. Safrankova, and Z. Nemecek (2003), Earth's bow shock and
- magnetopause in the case of a field-aligned upstream flow: Observation and model comparison,
- 823 *J. Geophys. Res. Sp. Phys.*, 108, 1 10, doi:10.1029/2002JA009697.
- Meurant, M., J.-C. Gérard, B. Hubert, V. Coumans, C. Blockx, N. Østgaard, and S. B. Mende
- 825 (2003), Dynamics of global scale electron and proton precipitation induced by a solar wind
- pressure pulse, *Geophys. Res. Lett.*, 30, 2032, doi:10.1029/2003GL018017.
- Min, K., J. Lee, K. Keika, and W. Li (2012), Global distribution of EMIC waves derived from
- 828 THEMIS observations, *J. Geophys. Res.*, 117, A05219, doi:10.1029/2012JA017515.
- Mursula, K. (2007), Satellite observations of Pc 1 pearl waves: the changing paradigm, J. Atmos.
- 830 *Sol.-Terr. Phys.* 69, 1623-1634, doi:10.1016/j.jastp.2007.02.013
- Mursula, K., T. Bräysy, K. Niskala, and C. T. Russell (2001), Pc1 pearls revisited: Structured
- electromagnetic ion cyclotron waves on Polar satellite and on ground, J. Geophys. Res., 106,
- 833 29543–29553, doi:10.1029/2000JA003044.
- Newell, P. T., and J. W. Gjerloev (2011), Evaluation of SuperMAG auroral electrojet indices as
- indicators of substorms and auroral power, J. Geophys. Res., 116, A12211,
- 836 doi:10.1029/2011JA016779.

- 837 Park, J.-S., K.-H. Kim, K. Shiokawa, D.-H. Lee, E. Lee, H.-J. Kwon, H. Jin, and G. Jee (2016),
- EMIC waves observed at geosynchronous orbit under quiet geomagnetic conditions $(Kp \le 1)$, J.
- 839 Geophys. Res. Space Physics, 121, 1377–1390, doi:10.1002/2015JA021968.
- Reeves, G. D., and M. G. Henderson (2001), The storm-substorm relationship: Ion injections in
- geosynchronous measurements and composite energetic neutral atom images, J. Geophys. Res.,
- 842 106, 5833 15, 544, doi:10.1029/2001JA003017.
- Saikin, A. A., J.-C. Zhang, R. C. Allen, C. W. Smith, L. M. Kistler, H. E. Spence, R. B. Torbert,
- 844 C. A. Kletzing, and V. K. Jordanova (2015), The occurrence and wave properties of H+-, He+-,
- and O+-band EMIC waves observed by the Van Allen Probes, J. Geophys. Res. Sp. Phys., 120, 1
- 846 16, doi:10.1029/JA021358.
- Saikin, A. A., J. Zhang, C. W. Smith, H. E. Spence, R. B. Torbert, and C. A. Kletzing (2016),
- The dependence on geomagnetic conditions and solar wind dynamic pressure of the spatial
- distributions of EMIC waves observed by the Van Allen Probes, J. Geophys. Res., 121,
- 850 doi:10.10002/2016JA022523.
- 851 Spence, H. E., et al. (2013), Science goals and overview of the Radiation Belt Storm Probes
- 852 (RBSP) Energetic Particle, Composition, and Thermal Plasma (ECT) suite on NASA's Van
- 853 Allen Probes mission, *Space Sci. Rev.*, 179, 311 336, doi:10.1007/s11214-013-0007-5.
- 854 Søraas, F., K., M. Laundal, and M. Usanova (2013), Coincident particle and optical observations
- of nightside subauroral proton precipitation, J. Geophys. Res. Space Physics, 118, 1112–1122,
- 856 doi:10.1002/jgra.50172.

- Tsurutani, B. T., and E. J. Smith (1977), Two types of magnetospheric ELF chorus and their
- substorm dependences, *J. Geophys. Res.*, 82(32), 5112 5128, doi:10.1029/JA082i032p05112.
- Usanova, M. E., I. R. Mann, I. J. Rae, Z. C. Kale, V. Angelopoulos, J. W. Bonnell, K.-H.
- Glassmeier, H. U. Auster, and H. J. Singer (2008), Multipoint observations of magnetospheric
- compression-related EMIC Pc1 waves by THEMIS and CARISMA, Geophys. Res. Letters, 35,
- 862 L17S25, doi:10.1029/2008GL034458.
- Usanova, M. E., I. R. Mann, Z. C. Kale, I. J. Rae, R. D. Sydora, M. Sandanger, F. Soraas, K.-H.
- Glassmeier, K.-H. Fornacon, H. Matsui, P. A. Puhl-Quinn, A. Masson, and X. Vallières (2010),
- 865 Conjugate ground and multisatellite observations of compression-related EMIC Pc1 waves and
- associated proton precipitation, J. Geophys. Res. Sp. Phys., 115, A07208,
- 867 doi:10.1029/2009JA014935.
- Usanova, M. E., I. R. Mann, J. Bortnik, L. Shao, and V. Angelopoulos (2012), THEMIS
- observations of electromagnetic ion cyclotron wave occurrence: Dependence on AE, SYMH, and
- solar wind dynamic pressure, *J. Geophys. Res.*, 117, 1 13, doi:10.1029/2012JA018049.
- Usanova, M. E., F. Darrouzet, I. R. Mann, and J. Bortnik (2013), Statistical analysis of EMIC
- waves in plasmaspheric plumes from Cluster observations, J. Geophys. Res., 118, 4946 4951,
- 873 doi:10.1002/jgra.50464.
- Usanova, M. E., A. Drozdov, K. Orlova, I. R. Mann, Y. Shprits, M. T. Rovertson, D. L. Turner,
- D. K. Milling, A. Kale, D. N. Baker, S. A. Thaller, G. D. Reeves, H. E. Spence, C. Kletzing, and
- J. Wygant (2014), Effect of EMIC waves on relativistic and ultrarelativistic electron populations:
- 677 Ground-based and Van Allen Probes observations, *Geophys. Res. Lett.*, 41, 1375 1381,
- 878 doi:10.1002/2013GL059024.

- Usanova, M. E., I. R. Mann, and F. Darrouzet (2016), EMIC waves in the inner magnetosphere,
- in Low-Frequency Waves in Space Plasmas, Geophysical Monograph 216, edited by A. Keiling,
- D.-H. Lee, and V. Nakariakov, Washington, DC: American Geophysical Union, 65-78.
- Wang, D., Z. Yuan, X. Yu, X. Deng, M. Zhou, S. Huang, H. Li, Z. Wang, Z. Qiao, C. A.
- Kletzing, and J. R. Wygant (2015), Statistical characteristic of EMIC waves: Van Allen Probe
- observations. J. Geophys. Res. Space Physics, doi: 10.1002/2015JA021089.
- Wentworth, R. C. (1964), Enhancement of hydromagnetic emissions after geomagnetic storms,
- 886 *J. Geophys. Res.*, 69, 2291 2298.
- Wygant, J. R., et al. (2013), The electric field and waves instruments on the Radiation Belt Storm
- 888 Probes mission, *Space Sci. Rev.*, 179, 183 220, doi:10.1007/s11214-013-0013-7.
- Zhang, Y., L. Paxton, D. Morrison, B. Wolven, H. Kil, and S. Wing (2005), Nightside detached
- auroras due to precipitating protons/ions during intense magnetic storms, J. Geophys. Res., 110,
- 891 A02206, doi:10.1029/2004JA010498.
- Zhang, Y., L. J. Paxton, and Y. Zheng (2008), Interplanetary shock induced ring current auroras,
- 893 *J. Geophys. Res.*, 113, A01212, doi:10.1029/2007JA012554
- Zhao, H., et al. (2015), The evolution of ring current ion energy density and energy content
- during geomagnetic storms based on Van Allen Probes measurements, J. Geophys. Res. Space
- 896 *Physics*, 120, 7493–7511, doi:10.1002/2015JA021533.

Table 1. Total number of events in this study, categorized by location relative to the plasmapause, by local time sector, and by storm phase.

PP Location	# of events
Inside	19
At	20
Outside	16
Total:	55

MLT Sector	# of events
0-6	17
6-12	23
12-18	22
18-24	16
Total:	78

Storm Phase	# of events
Main	9
Recovery	18
Pre-Onset	1
Quiet	44
Compressional	6
Total:	78

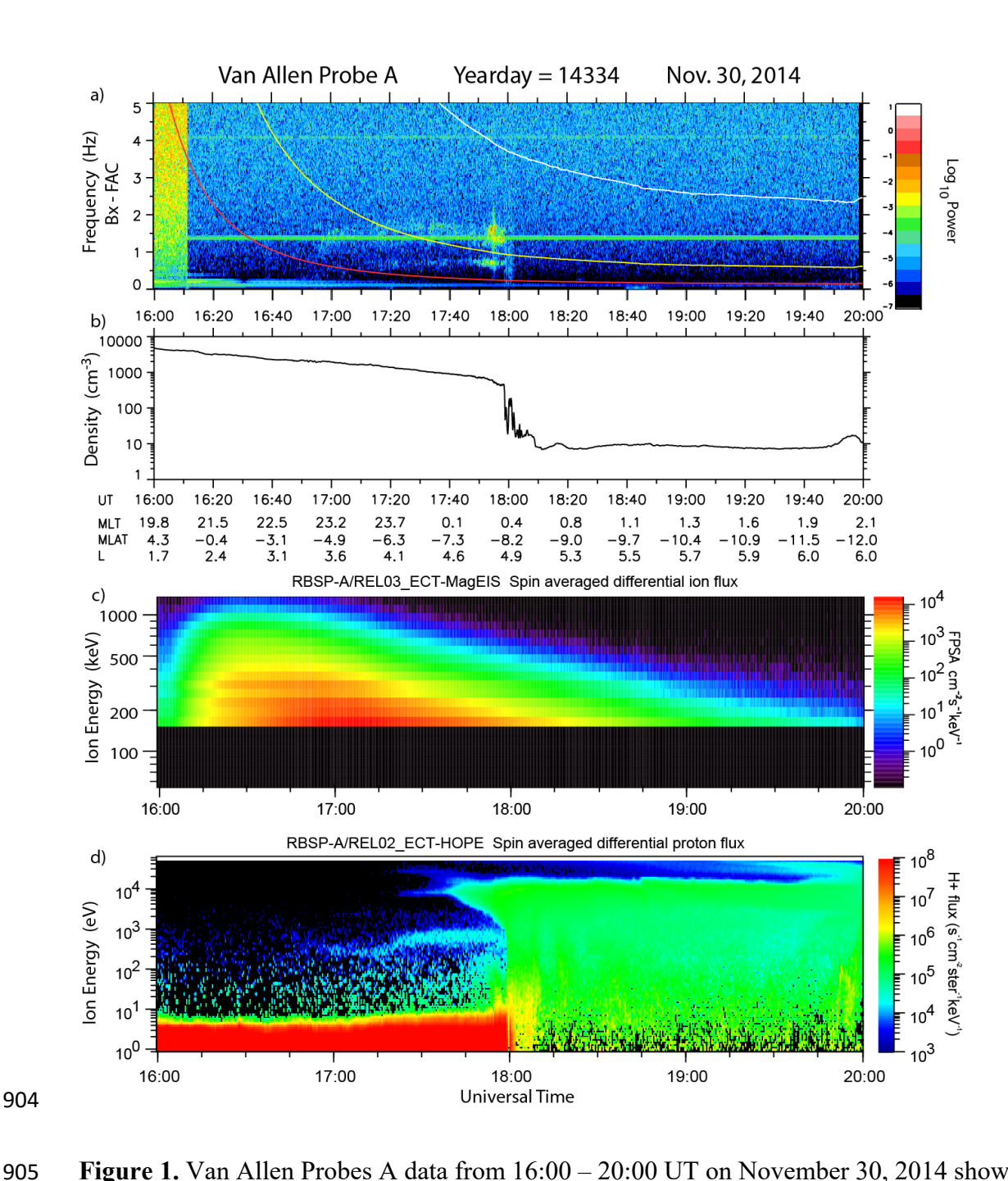


Figure 1. Van Allen Probes A data from 16:00 – 20:00 UT on November 30, 2014 showing an EMIC wave event observed during an outbound pass one hour after a strong substorm injection. The four panels show a Fourier spectrogram of EMFISIS magnetic field data in field-aligned coordinates (panel a), EFW electron density data (panel b), ring current proton fluxes measured by the HOPE instruments (panel c), and MagEIS ion fluxes (panel d), respectively.

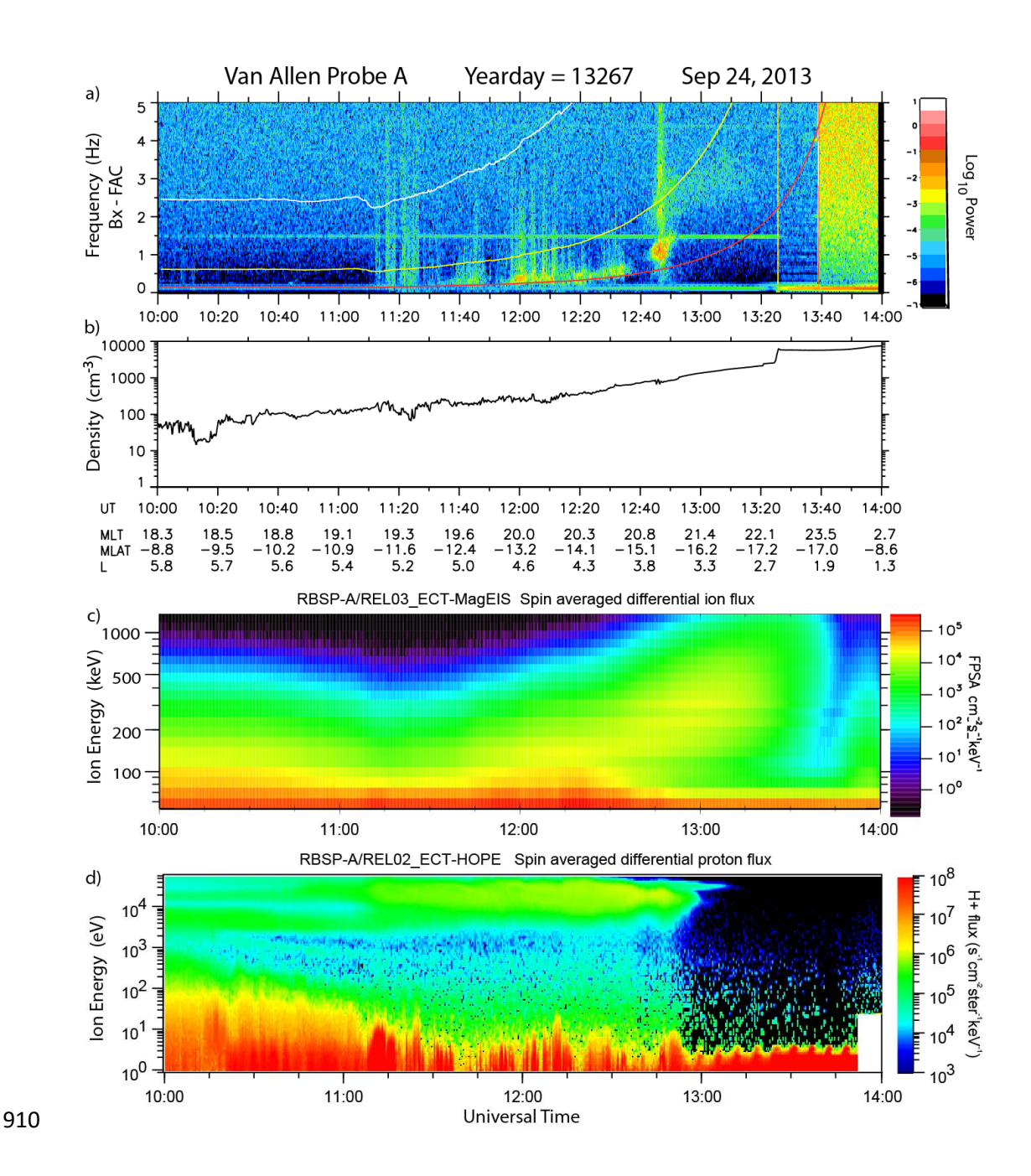


Figure 2. Van Allen Probes A data from 10:00 - 14:00 UT on September 24, 2013, as in Figure 1, for an EMIC wave event observed during an inbound pass from ~ 19 to ~ 22 hours MLT as the spacecraft passed from L = 5 to 3.5 during the main phase of a weak storm.

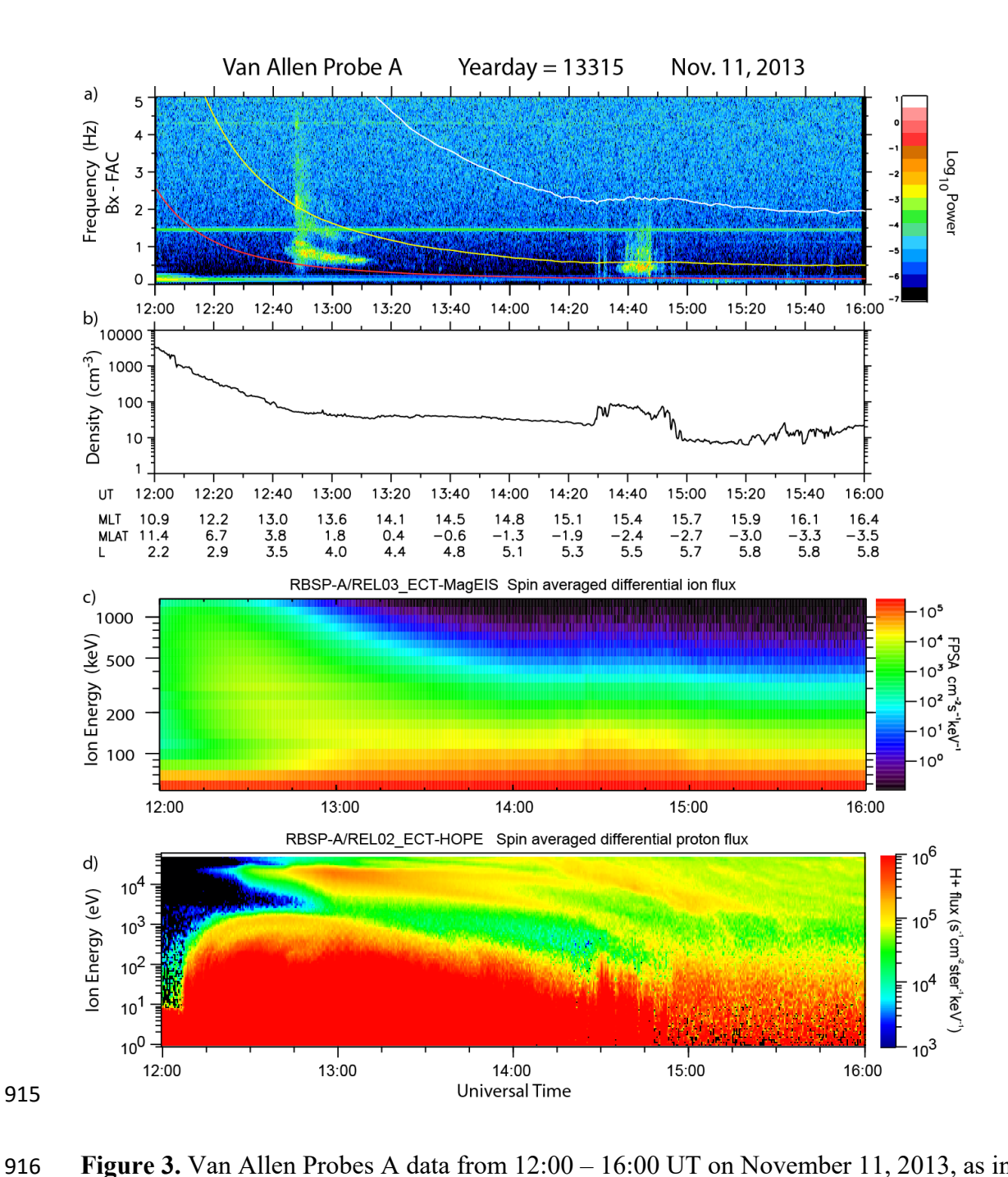


Figure 3. Van Allen Probes A data from 12:00 - 16:00 UT on November 11, 2013, as in Figure 1, for an EMIC wave event observed during an outbound pass in the afternoon sector during the early recovery phase of a magnetic storm.

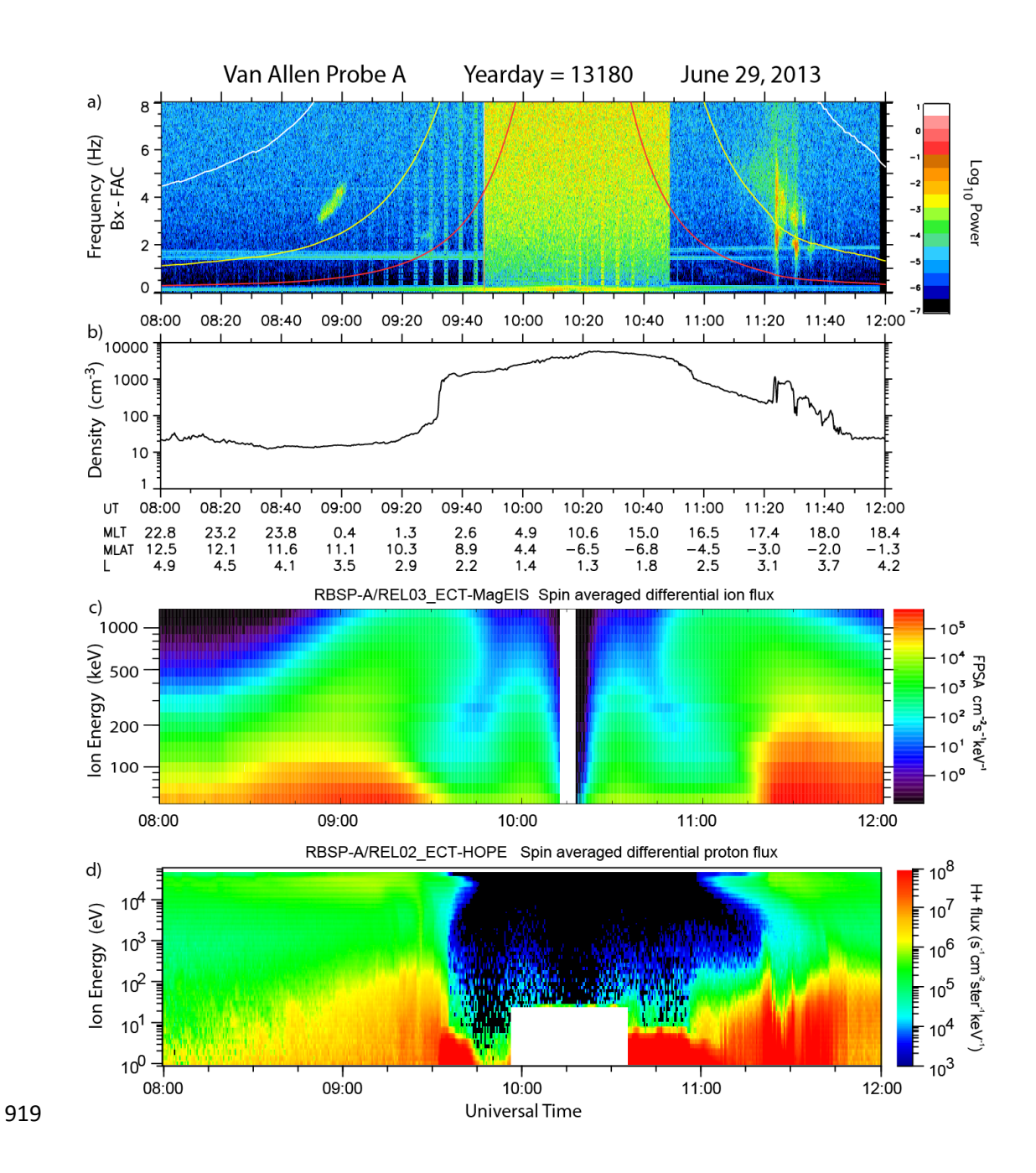


Figure 4. Van Allen Probes A data from 08:00 - 12:00 UT on June 29, 2013, as in Figure 1, for an EMIC wave event observed during the early recovery phase of the magnetic storm.

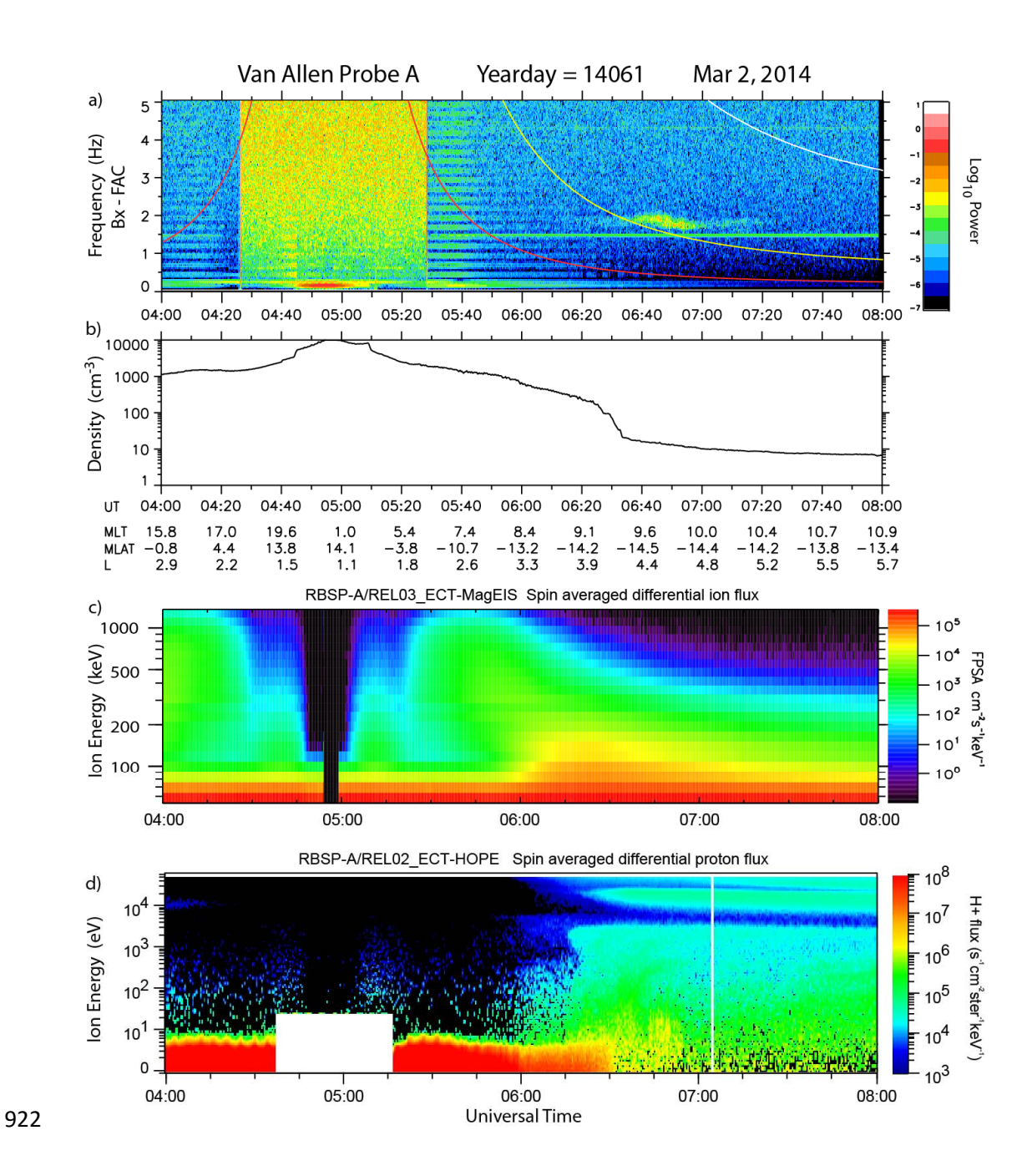


Figure 5. Van Allen Probes A data from 04:00 - 08:00 UT on March 2, 2014, as in Figure 1, for an EMIC wave event observed two days after the end of the main phase of a magnetic storm.

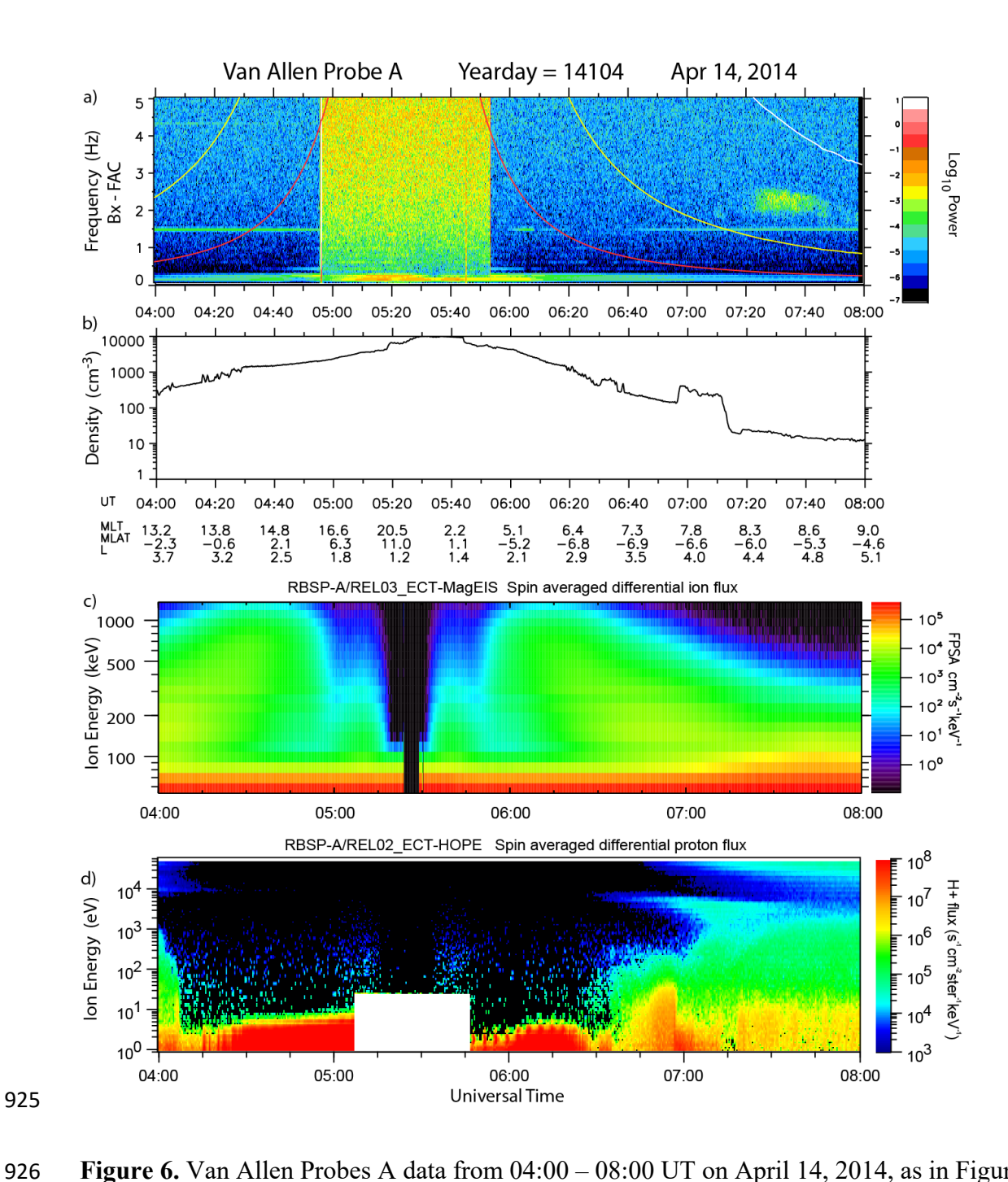


Figure 6. Van Allen Probes A data from 04:00 - 08:00 UT on April 14, 2014, as in Figure 1, for an EMIC wave event observed two days after the main phase of a magnetic storm.

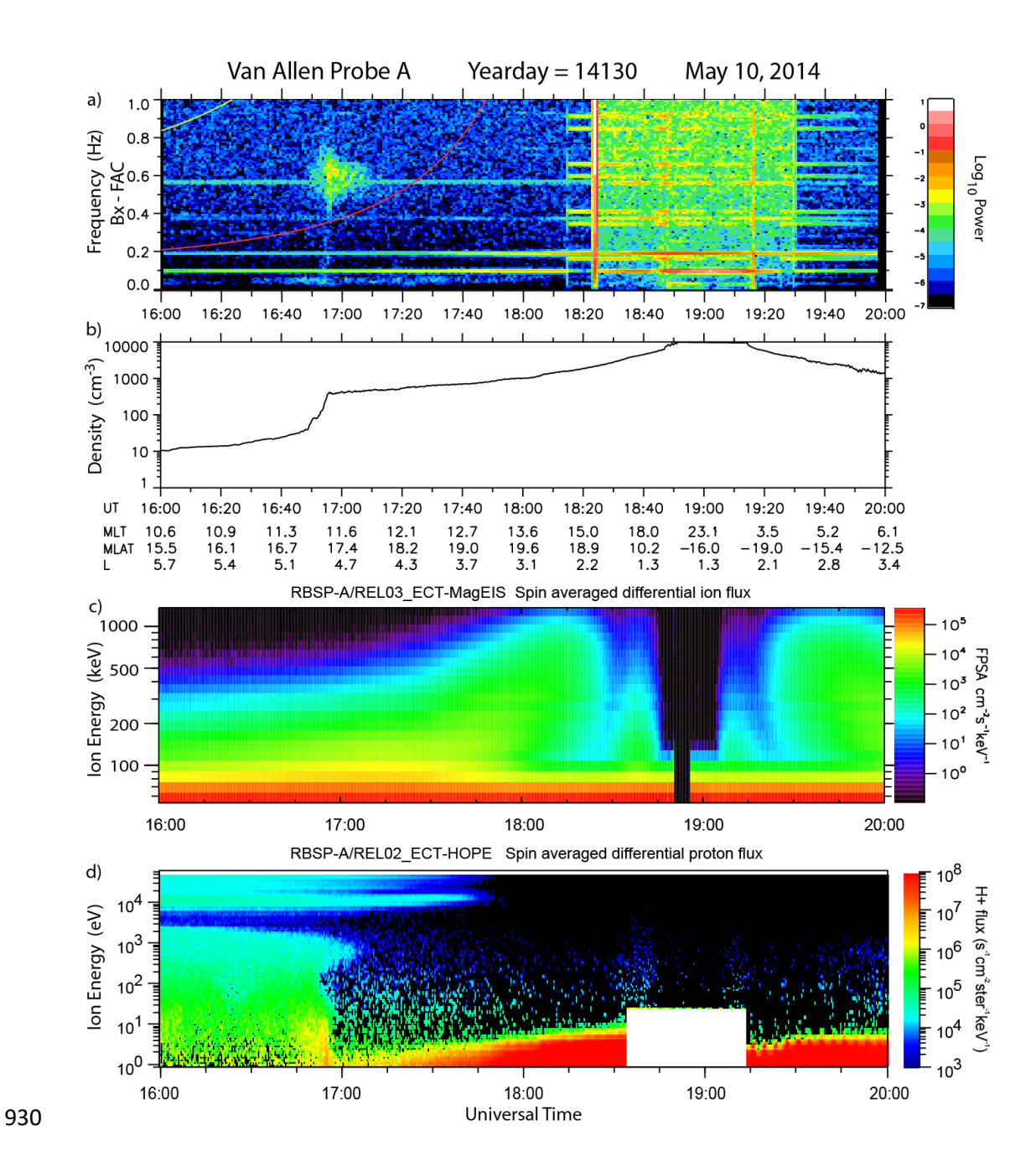


Figure 7. Van Allen Probes A data from 16:00 - 20:00 UT on May 10, 2014, as in Figure 1, for an EMIC wave event observed during an inbound crossing of the inner edge of the plasmapause at L = 4.8 near local noon, two days after the main phase of a magnetic storm.

Distribution of Waves Relative to the Plasmapause

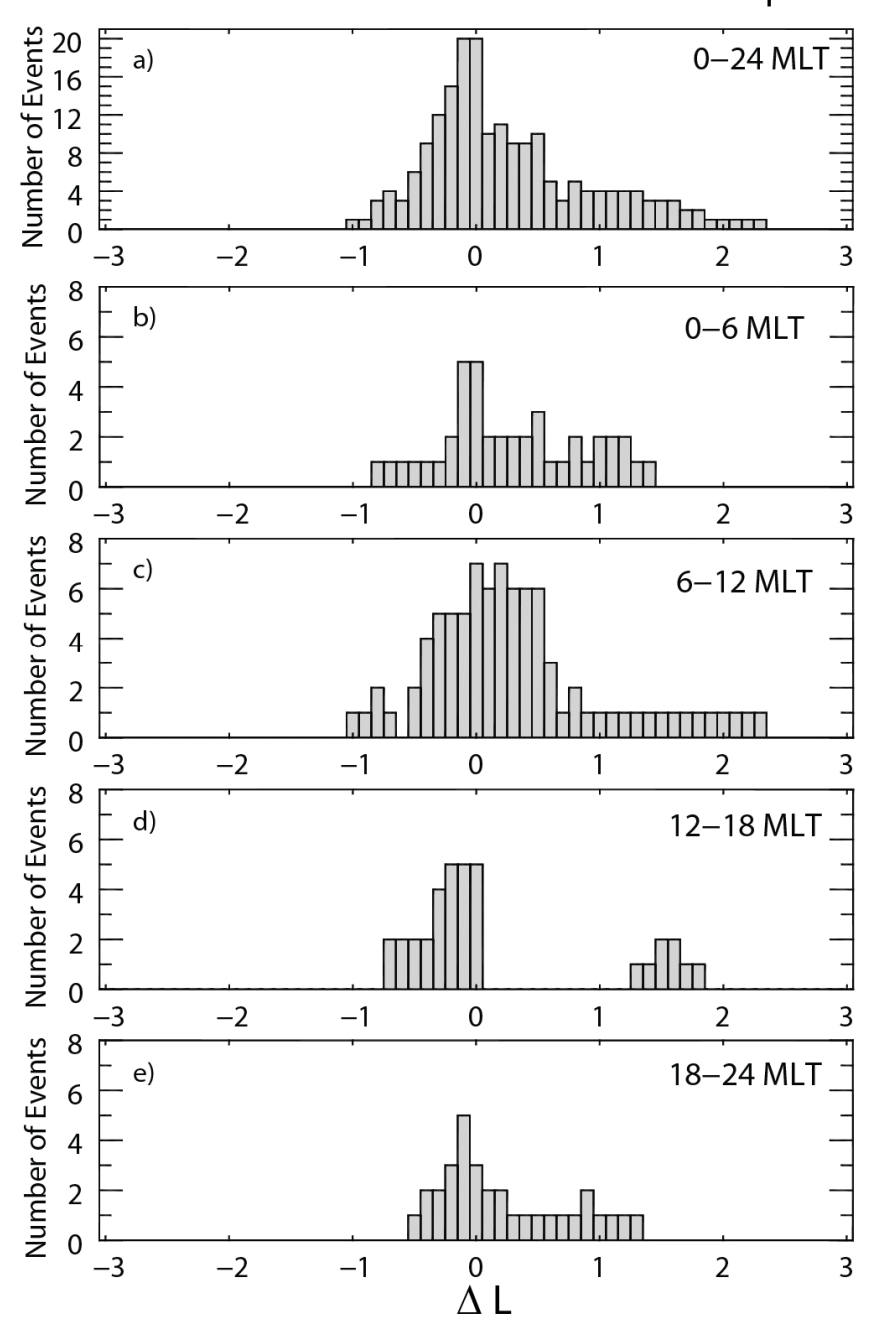
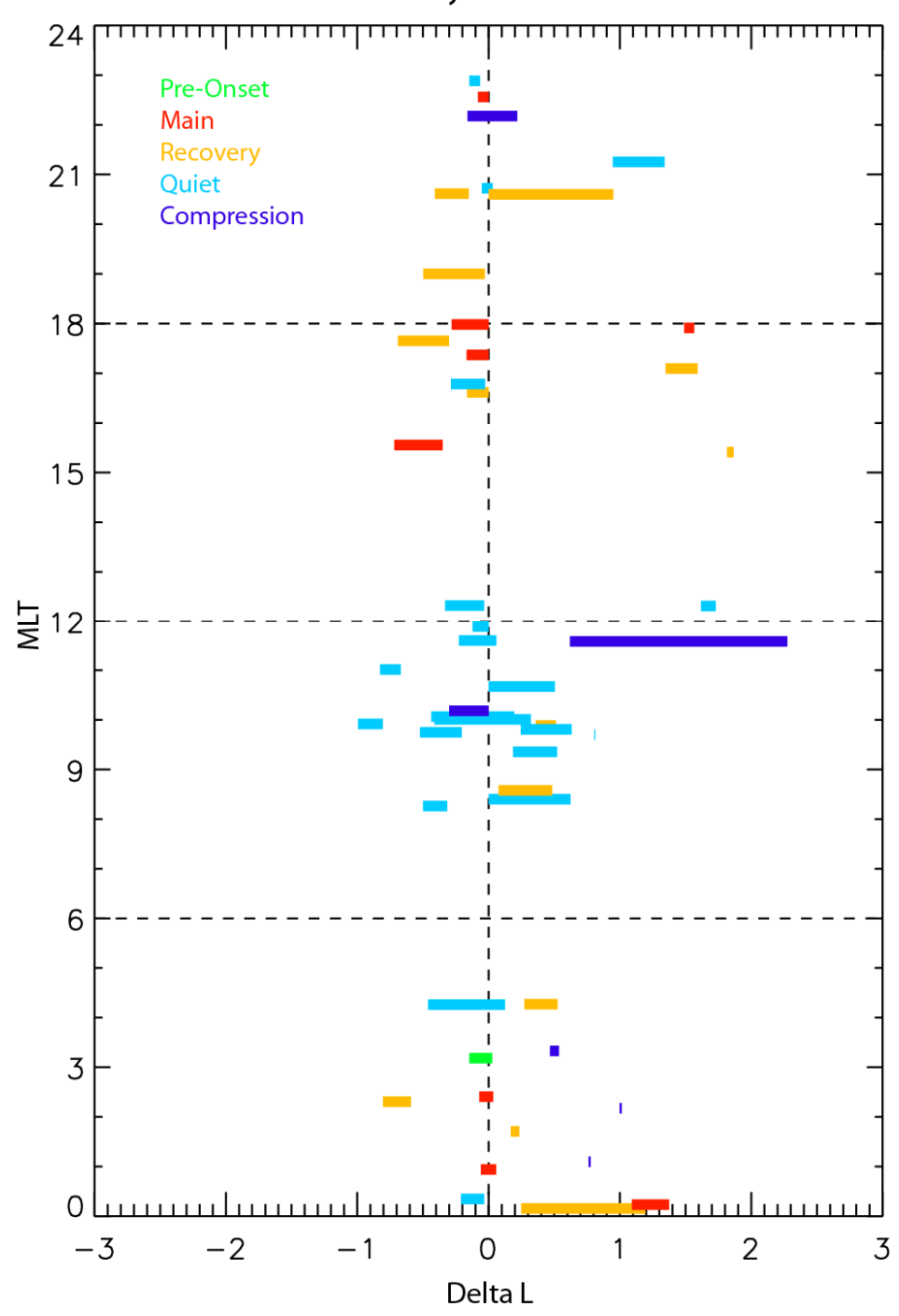


Figure 8. Local time quadrant distribution of EMIC waves in ΔL from the observed plasmapause in bins of 0.1 L. Individual events often spanned several bins.

Local Time Distribution of EMIC Events H band H and He bands He bands Number of Events Inside PP 0 0 Number of Events At PP Number of Events Outside PP 0 0 Number of Events Other MLT MLT MLT

Figure 9. The numbers of events inside, at, or outside the plasmapause, or in a fourth category "other", which include complex density structures, plumes, and passes with no sharp plasmapause density gradient, out to apogee near L = 5.9, all as a function of local time quadrant and band: H-band, He-band, or both.

Transverse Waves Relative to the Plasmapause Sorted by Storm Phase



946

947

Figure 10. Distribution of EMIC waves as a function of MLT (vertical axis) and ΔL from the observed PP, color-coded according to storm phase.

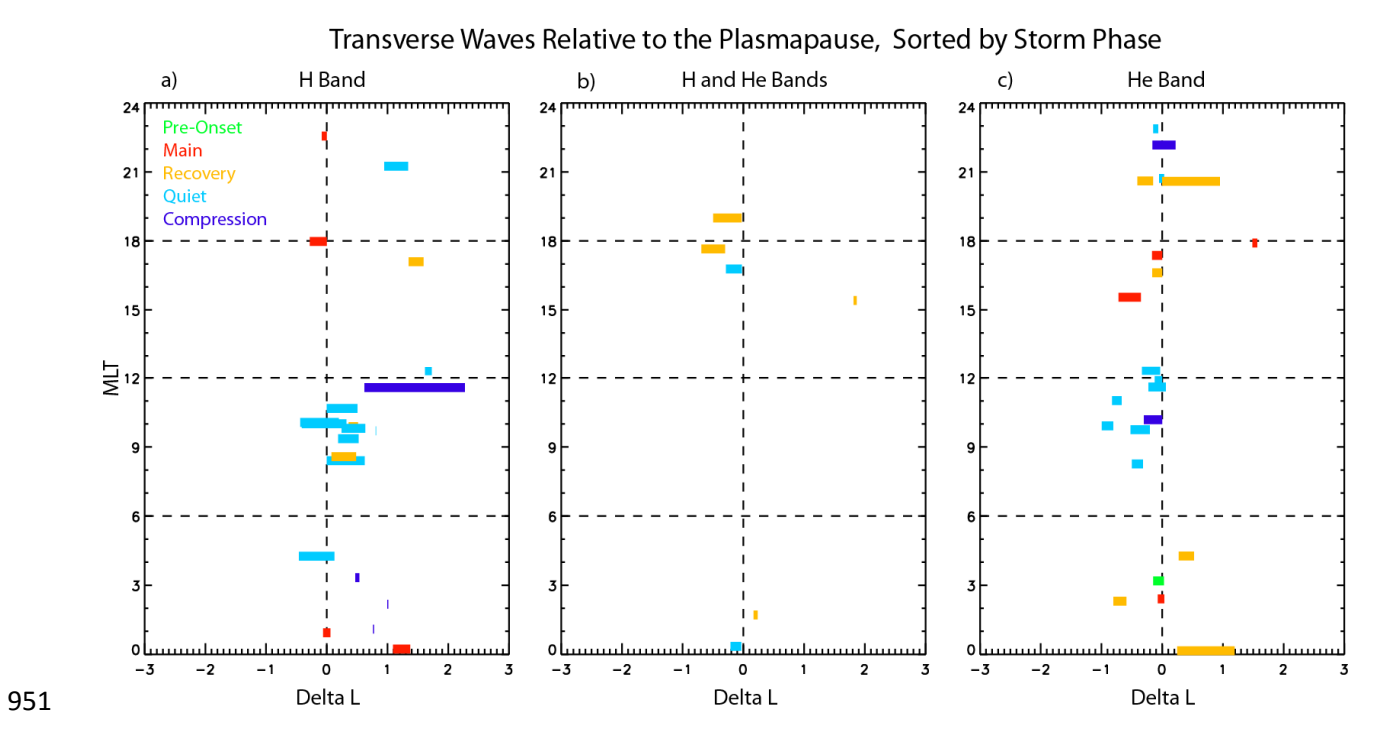


Figure 11. Distribution of EMIC waves as a function of MLT, ΔL from the observed PP, and storm phase, as in Figure 10, sorted by frequency band.

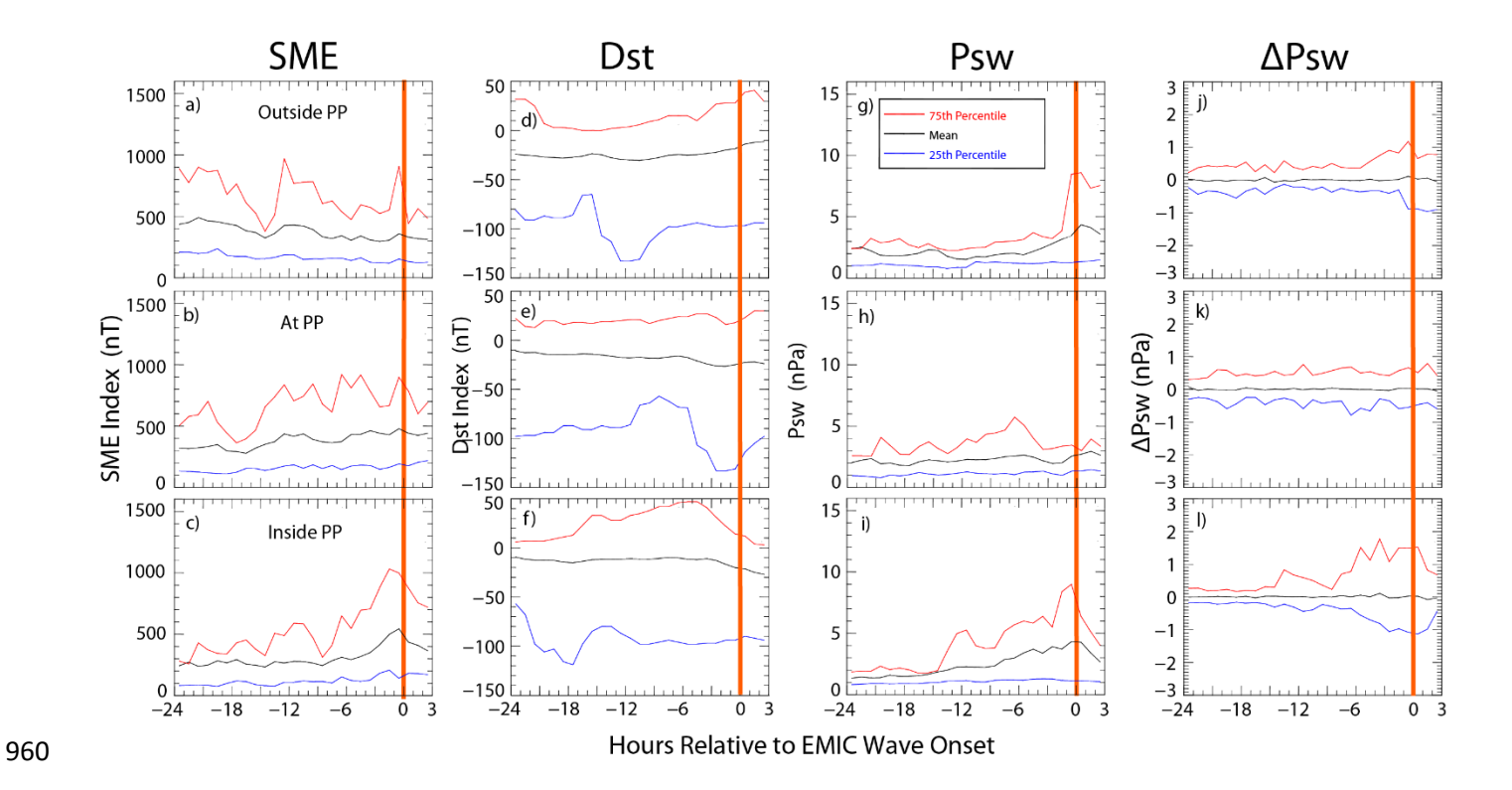


Figure 12. Superposed epoch plots showing the mean, 75th percentile, and 25th percentile of the SME index, Dst index, solar wind dynamic pressure (Psw), and 5-min variations in Psw during and before the 55 events for which there was a clear plasmapause structure, sorted by event location relative to the PP.

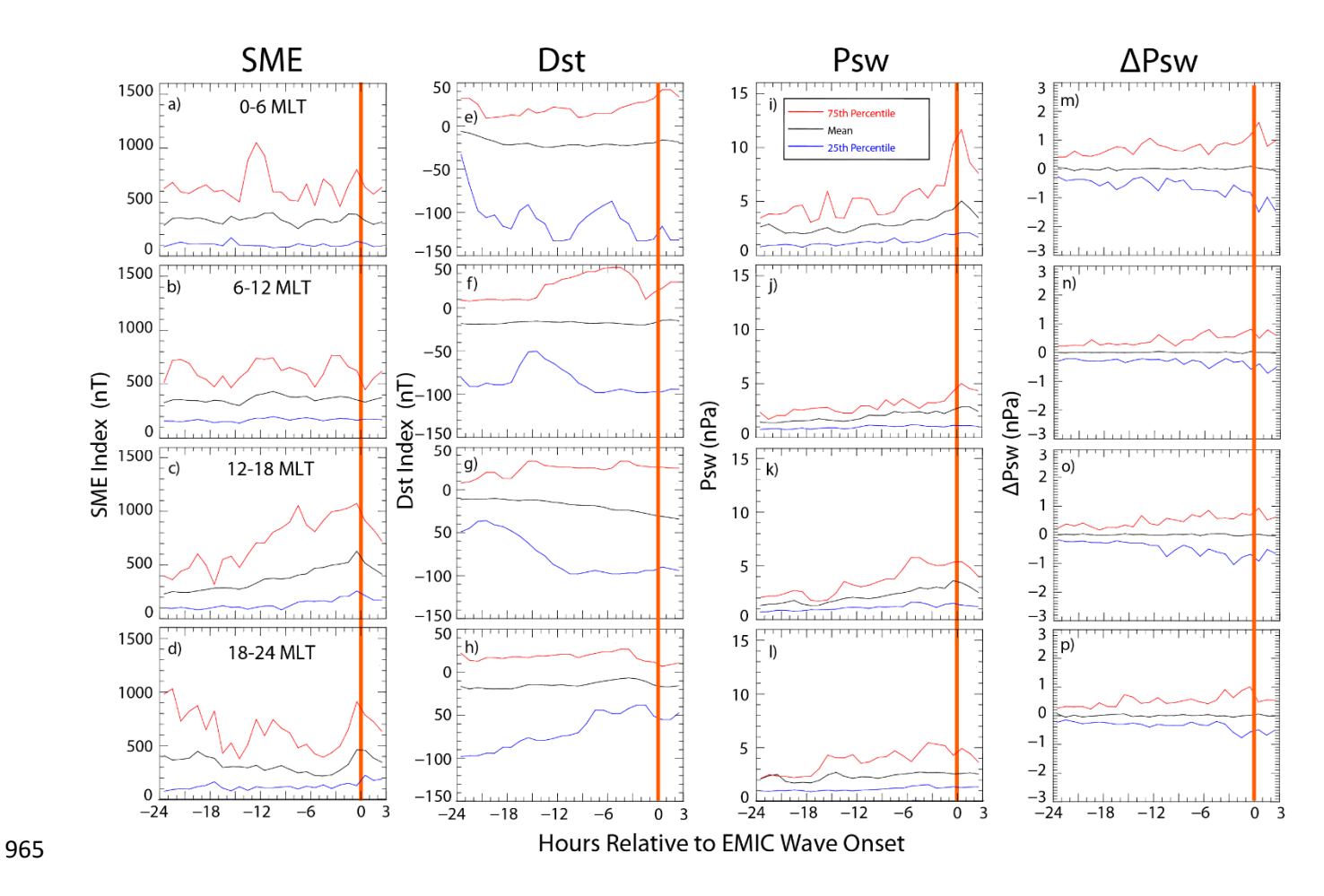


Figure 13. Superposed epoch plots showing the mean, 75th percentile, and 25th percentile of the SME index, Dst index, solar wind dynamic pressure (Psw), and 5-min variations in Psw during and before the 78 wave events included in this study, sorted by magnetic local time sector (0-6, 6-12, 12-18, and 18-24 h MLT).

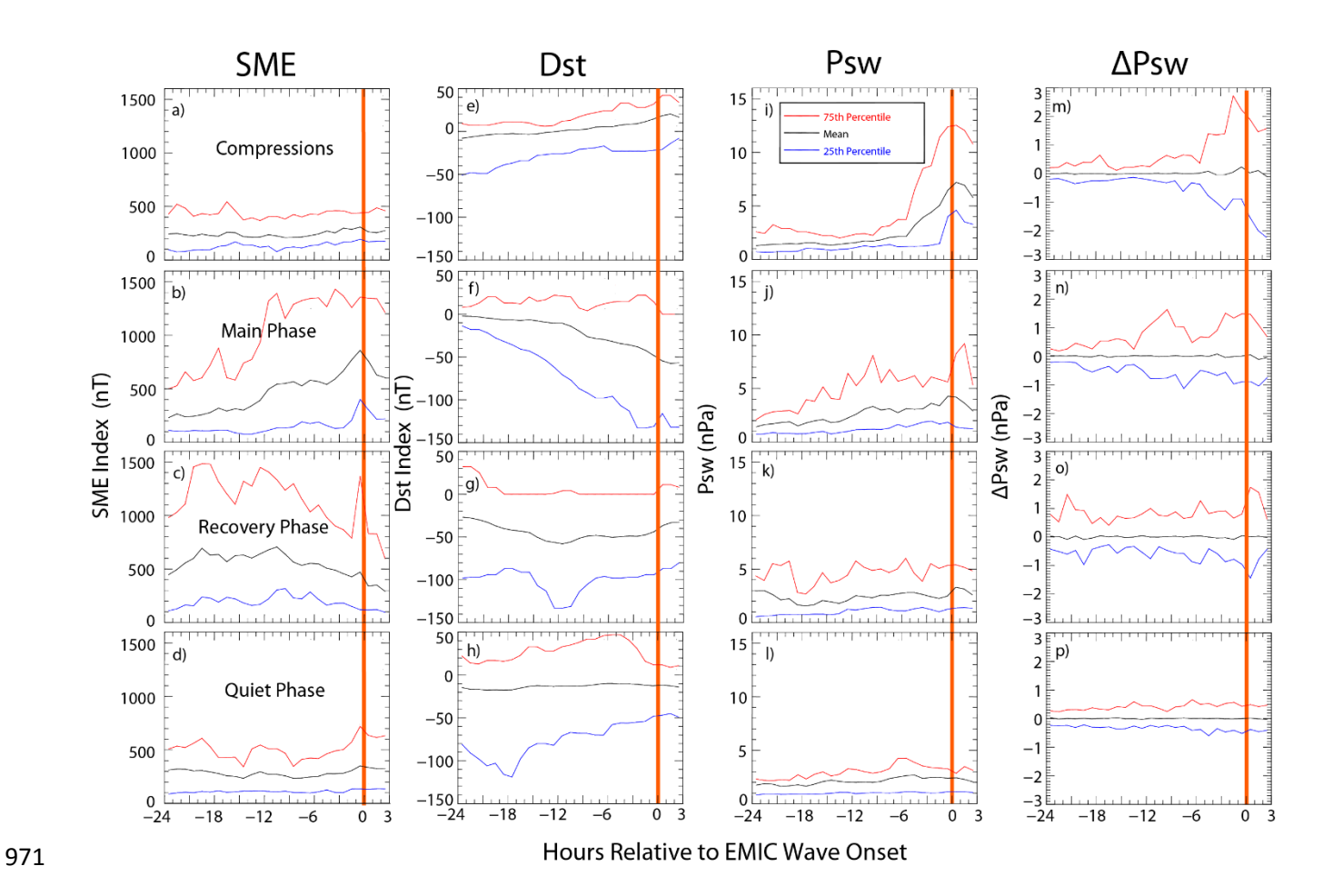


Figure 14. Superposed epoch plots showing the mean, 75th percentile, and 25th percentile of the SME index, Dst index, solar wind dynamic pressure (Psw), and 5-min variations in Psw during and before the 78 wave events included in this study, sorted by magnetic storm phase (compressions, main phase, recovery phase, and quiet).

Transverse Waves Relative to the Plasmapause Sorted by Amplitude

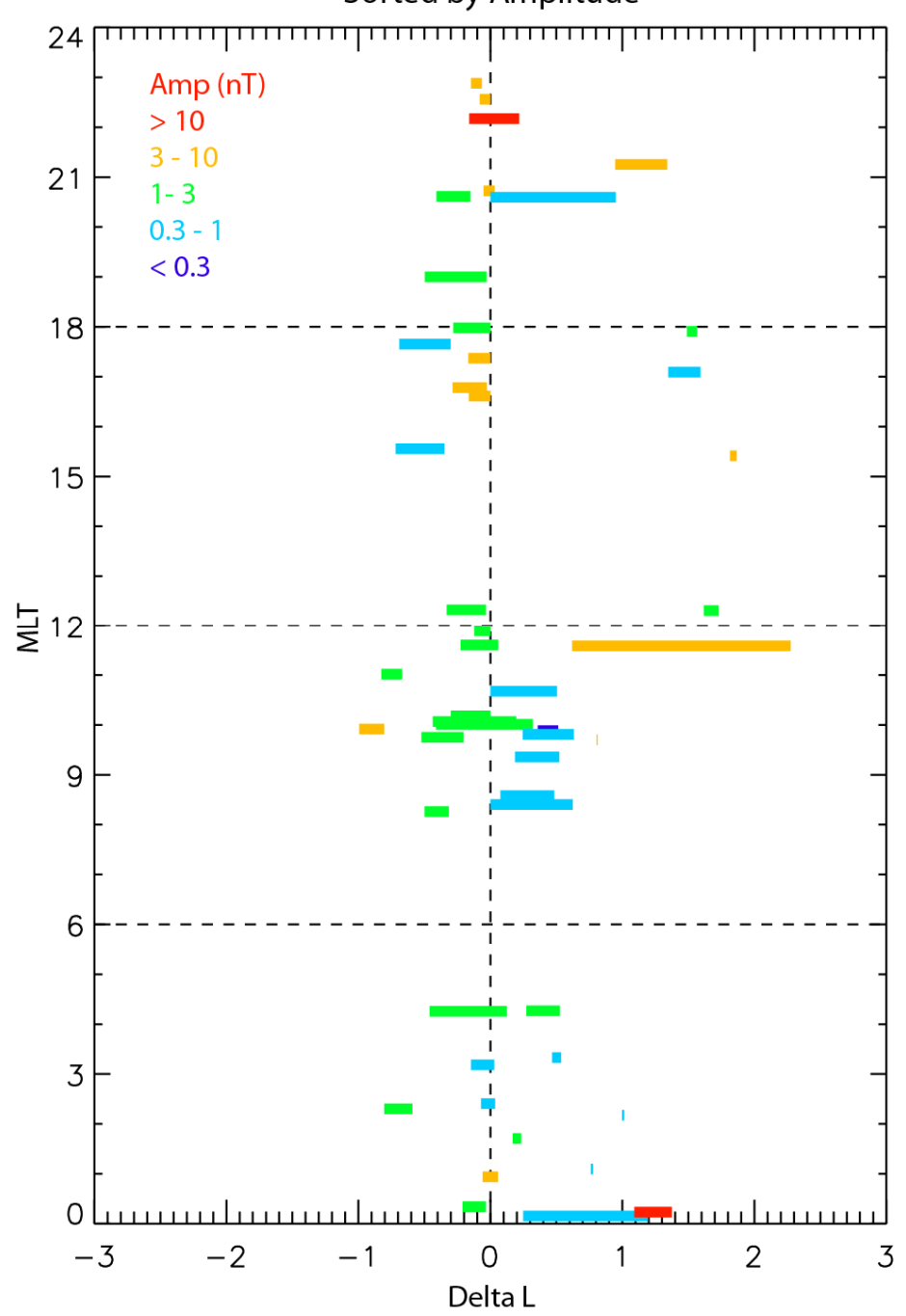


Figure 15. Distribution of EMIC waves as a function of MLT (vertical axis) and ΔL from the observed plasmapause, color-coded according to the transverse component RMS amplitudes (nT).

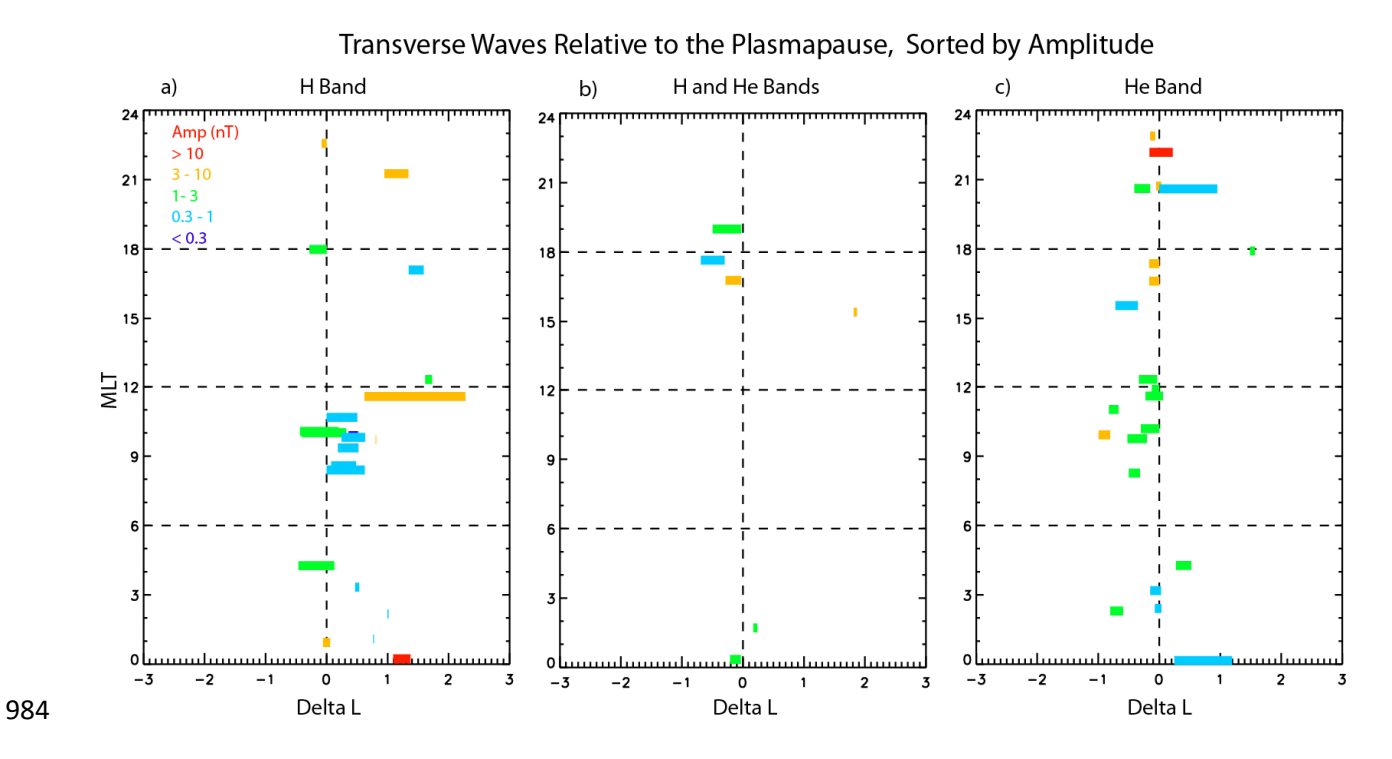


Figure 16. Distribution of EMIC waves as a function of MLT ΔL from the observed PP, and transverse RMS amplitudes, as in Figure 15, sorted by frequency band.